

28. PARTICLE DETECTORS

Revised 2003 (see the various sections for authors).

In this section we give various parameters for common detector components. The quoted numbers are usually based on typical devices, and should be regarded only as rough approximations for new designs. More detailed discussions of detectors and their underlying physics can be found in books by Ferbel [1], Grupen [2], Kleinknecht [3], Knoll [4], and Green [5]. In Table 28.1 are given typical spatial and temporal resolutions of common detectors.

Table 28.1: Typical spatial and temporal resolutions of common detectors. Revised September 2003 by R. Kadel (LBNL).

Detector Type	Accuracy (rms)	Resolution Time	Dead Time
Bubble chamber	10–150 μm	1 ms	50 ms ^a
Streamer chamber	300 μm	2 μs	100 ms
Proportional chamber	50–300 $\mu\text{m}^{b,c,d}$	2 ns	200 ns
Drift chamber	50–300 μm	2 ns ^e	100 ns
Scintillator	—	100 ps/n ^f	10 ns
Emulsion	1 μm	—	—
Liquid Argon Drift [Ref. 6]	$\sim 175\text{--}450 \mu\text{m}$	$\sim 200 \text{ ns}$	$\sim 2 \mu\text{s}$
Gas Micro Strip [Ref. 7]	30–40 μm	< 10 ns	—
Resistive Plate chamber [Ref. 8]	$\lesssim 10 \mu\text{m}$	1–2 ns	—
Silicon strip	pitch/(3 to 7) ^g	h	h
Silicon pixel	2 μm^i	h	h

^a Multiple pulsing time.

^b 300 μm is for 1 mm pitch.

^c Delay line cathode readout can give $\pm 150 \mu\text{m}$ parallel to anode wire.

^d wirespacing/ $\sqrt{12}$.

^e For two chambers.

^f n = index of refraction.

^g The highest resolution (“7”) is obtained for small-pitch detectors ($\lesssim 25 \mu\text{m}$) with pulse-height-weighted center finding.

^h Limited by the readout electronics [9]. (Time resolution of $\leq 25 \text{ ns}$ is planned for the ATLAS SCT.)

ⁱ Analog readout of 34 μm pitch, monolithic pixel detectors.

2 28. Particle detectors

28.1. Organic scintillators

Revised September 2001 by K.F. Johnson (FSU).

Organic scintillators are broadly classed into three types, crystalline, liquid, and plastic, all of which utilize the ionization produced by charged particles (see the section on “Passage of particles through matter” (Sec. 27.2) of this *Review*) to generate optical photons, usually in the blue to green wavelength regions [10]. Plastic scintillators are by far the most widely used. Crystal organic scintillators are practically unused in high-energy physics.

Densities range from 1.03 to 1.20 g cm⁻³. Typical photon yields are about 1 photon per 100 eV of energy deposit [11]. A one-cm-thick scintillator traversed by a minimum-ionizing particle will therefore yield $\approx 2 \times 10^4$ photons. The resulting photoelectron signal will depend on the collection and transport efficiency of the optical package and the quantum efficiency of the photodetector.

Plastic scintillators do not respond linearly to the ionization density. Very dense ionization columns emit less light than expected on the basis of dE/dx for minimum-ionizing particles. A widely used semi-empirical model by Birks posits that recombination and quenching effects between the excited molecules reduce the light yield [12]. These effects are more pronounced the greater the density of the excited molecules. Birks’ formula is

$$\frac{d\mathcal{L}}{dx} = \mathcal{L}_0 \frac{dE/dx}{1 + k_B dE/dx},$$

where \mathcal{L} is the luminescence, \mathcal{L}_0 is the luminescence at low specific ionization density, and k_B is Birks’ constant, which must be determined for each scintillator by measurement.

Decay times are in the ns range; rise times are much faster. The combination of high light yield and fast response time allows the possibility of sub-ns timing resolution [13]. The fraction of light emitted during the decay “tail” can depend on the exciting particle. This allows pulse shape discrimination as a technique to carry out particle identification. Because of the hydrogen content (carbon to hydrogen ratio ≈ 1) plastic scintillator is sensitive to proton recoils from neutrons. Ease of fabrication into desired shapes and low cost has made plastic scintillators a common detector component. Recently, plastic scintillators in the form of scintillating fibers have found widespread use in tracking and calorimetry [14].

28.1.1. *Scintillation mechanism* :

Scintillation: A charged particle traversing matter leaves behind it a wake of excited molecules. Certain types of molecules, however, will release a small fraction ($\approx 3\%$) of this energy as optical photons. This process, scintillation, is especially marked in those organic substances which contain aromatic rings, such as polystyrene (PS) and polyvinyltoluene (PVT). Liquids which scintillate include toluene and xylene.

Fluorescence: In fluorescence, the initial excitation takes place via the absorption of a photon, and de-excitation by emission of a longer wavelength photon. Fluors are used as “wavelength shifters” to shift scintillation light to a more convenient wavelength. Occurring in complex molecules, the absorption and emission are spread out over a wide band of

photon energies, and have some overlap, that is, there is some fraction of the emitted light which can be re-absorbed [15]. This “self-absorption” is undesirable for detector applications because it causes a shortened attenuation length. The wavelength difference between the major absorption and emission peaks is called the Stokes’ shift. It is usually the case that the greater the Stokes’ shift, the smaller the self absorption—thus, a large Stokes’ shift is a desirable property for a fluor (aka the “Better red than dead” strategy).

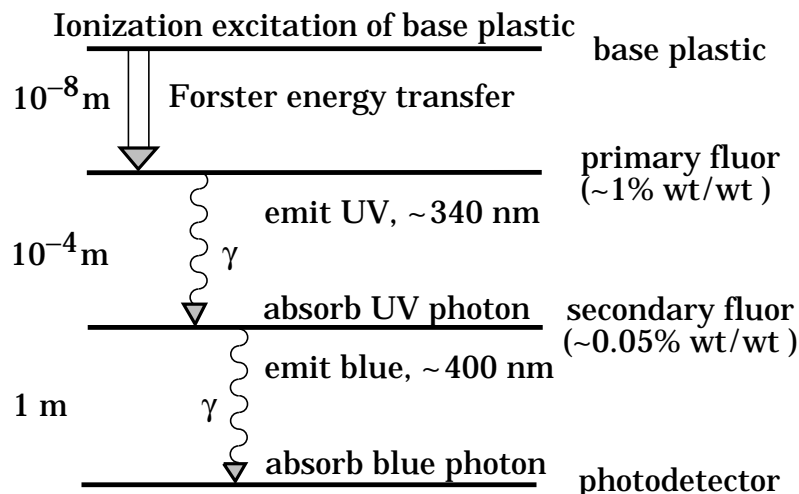


Figure 28.1: Cartoon of scintillation “ladder” depicting the operating mechanism of plastic scintillator. Approximate fluor concentrations and energy transfer distances for the separate sub-processes are shown.

Scintillators: The plastic scintillators used in high-energy physics are binary or ternary solutions of selected fluors in a plastic base containing aromatic rings. (See the appendix in Ref. 16 for a comprehensive list of components.) Virtually all plastic scintillators contain as a base either PVT or PS. PVT-based scintillator can be up to 50% brighter. The fluors must satisfy additional conditions besides being fluorescent. They must be sufficiently stable, soluble, chemically inert, fast, radiation tolerant, and efficient.

Ionization in the plastic base produces UV photons with short attenuation length (several mm). Longer attenuation lengths are obtained by dissolving a “primary” fluor in high concentration (1% by weight) into the base, which is selected to efficiently re-radiate absorbed energy at wavelengths where the base is more transparent.

The primary fluor has a second important function. The decay time of the scintillator base material can be quite long—in pure polystyrene it is 16 ns, for example. The addition of the primary fluor in high concentration can shorten the decay time by an order of magnitude and increase the total light yield. At the concentrations used (1% and greater), the average distance between a fluor molecule and an excited base unit is around 100 Å, much less than a wavelength of light. At these distances the predominant mode of energy transfer from base to fluor is not the radiation of a photon, but a resonant dipole-dipole interaction, first described by Foerster, which strongly couples the base and fluor [17]. The strong coupling sharply increases the speed and the light yield of the plastic scintillators.

4 28. Particle detectors

Unfortunately, a fluor which fulfills other requirements is usually not completely adequate with respect to emission wavelength or attenuation length, so it is necessary to add yet another waveshifter (the “secondary” fluor), at fractional percent levels, and occasionally a third (not shown in Fig. 28.1).

External wavelength shifters: Light emitted from a plastic scintillator may be absorbed in a (nonscintillating) base doped with a wave-shifting fluor. Such wavelength shifters are widely used to aid light collection in complex geometries. The wavelength shifter must be insensitive to ionizing radiation and Cherenkov light. A typical wavelength shifter uses an acrylic base because of its good optical qualities, a single fluor to shift the light emerging from the plastic scintillator to the blue-green, and contains ultra-violet absorbing additives to deaden response to Cherenkov light.

28.1.2. Caveats and cautions: Plastic scintillators are reliable, robust, and convenient. However, they possess quirks to which the experimenter must be alert.

Aging and Handling: Plastic scintillators are subject to aging which diminishes the light yield. Exposure to solvent vapors, high temperatures, mechanical flexing, irradiation, or rough handling will aggravate the process. A particularly fragile region is the surface which can ‘craze’—develop microcracks—which rapidly destroy the capability of plastic scintillators to transmit light by total internal reflection. Crazing is particularly likely where oils, solvents, or *fingerprints* have contacted the surface.

Attenuation length: The Stokes’ shift is not the only factor determining attenuation length. Others are the concentration of fluors (the higher the concentration of a fluor, the greater will be its self-absorption); the optical clarity and uniformity of the bulk material; the quality of the surface; and absorption by additives, such as stabilizers, which may be present.

Afterglow: Plastic scintillators have a long-lived luminescence which does not follow a simple exponential decay. Intensities at the 10^{-4} level of the initial fluorescence can persist for hundreds of ns [10,18].

Atmospheric quenching: Plastic scintillators will decrease their light yield with increasing partial pressure of oxygen. This can be a 10% effect in an artificial atmosphere [19]. It is not excluded that other gases may have similar quenching effects.

Magnetic field: The light yield of plastic scintillators may be changed by a magnetic field. The effect is very nonlinear and apparently not all types of plastic scintillators are so affected. Increases of $\approx 3\%$ at 0.45 T have been reported [20]. Data are sketchy and mechanisms are not understood.

Radiation damage: Irradiation of plastic scintillators creates color centers which absorb light more strongly in the UV and blue than at longer wavelengths. This poorly understood effect appears as a reduction both of light yield and attenuation length. Radiation damage depends not only on the integrated dose, but on the dose rate, atmosphere, and temperature, before, during and after irradiation, as well as the

materials properties of the base such as glass transition temperature, polymer chain length, *etc.* Annealing also occurs, accelerated by the diffusion of atmospheric oxygen and elevated temperatures. The phenomena are complex, unpredictable, and not well understood [21]. Since color centers are less intrusive at longer wavelengths, the most reliable method of mitigating radiation damage is to shift emissions at every step to the longest practical wavelengths, *e.g.*, utilize fluors with large Stokes' shifts (aka the "Better red than dead" strategy).

28.1.3. *Scintillating and wavelength-shifting fibers:*

The clad optical fiber is an incarnation of scintillator and wavelength shifter (WLS) which is particularly useful [22]. Since the initial demonstration of the scintillating fiber (SCIFI) calorimeter [23], SCIFI techniques have become mainstream. SCIFI calorimeters are found, for example, in the $g - 2$ experiment at Brookhaven [24] and at KLOE; SCIFI trackers are found at CHORUS and DØ ; WLS readout is used in both ATLAS and CMS hadron calorimeters [25].

SCIFI calorimeters are fast, dense, radiation hard, and can have leadglass-like resolution. SCIFI trackers can handle high rates and are radiation tolerant, but the low photon yield at the end of a long fiber (see below) forces the use of very sophisticated photodetectors such as VLPC's, such as are used in DØ . WLS scintillator readout of a calorimeter allows a very high level of hermeticity since the solid angle blocked by the fiber on its way to the photodetector is very small. The sensitive region of scintillating fibers can be controlled by splicing them onto clear (non-scintillating/non-WLS) fibers.

A typical configuration would be fibers with a core of polystyrene-based scintillator or WLS (index of refraction $n = 1.59$), surrounded by a cladding of PMMA ($n = 1.49$) a few microns thick, or, for added light capture, with another cladding of fluorinated PMMA with $n = 1.42$, for an overall diameter of 0.5 to 1 mm. The fiber is drawn from a boule and great care is taken during production to ensure that the intersurface between the core and the cladding has the highest possible uniformity and quality, so that the signal transmission via total internal reflection has a low loss. The fraction of generated light which is transported down the optical pipe is denoted the capture fraction and is about 6% for the single-clad fiber and 10% for the double-clad fiber.

The number of photons from the fiber available at the photodetector is always smaller than desired, and increasing the light yield has proven difficult [26]. A minimum-ionizing particle traversing a high-quality 1 mm diameter fiber perpendicular to its axis will produce fewer than 2000 photons, of which about 200 are captured. Attenuation eliminates about 95% of these photons. DØ uses 0.775 mm diameter scintillating fibers in the tracker and obtains 9 photoelectrons with the VLPC reaching 85% quantum efficiency.

A scintillating or WLS fiber is often characterized by its "attenuation length," over which the signal is attenuated to $1/e$ of its original value. Many factors determine the attenuation length, including the importance of re-absorption of emitted photons by the polymer base or dissolved fluors, the level of crystallinity of the base polymer, and the quality of the total internal reflection boundary. Attenuation lengths of several meters are obtained by high quality fibers. However, it should be understood that the

6 28. Particle detectors

attenuation length is not necessarily a measure of fiber quality. Among other things, it is not constant with distance from the excitation source and it is wavelength dependent. So-called “cladding light” causes some of the distance dependence [27], but not all. The wavelength dependence is usually related to the higher re-absorption of shorter wavelength photons—once absorbed, re-emitted isotropically and lost with 90% probability—and to the lower absorption of longer wavelengths by polystyrene. Experimenters should be aware that measurements of attenuation length by a phototube with a bialkali photocathode, whose quantum efficiency drops below 10% at 480 nm, should not be naïvely compared to measurements utilizing a silicon photodiode, whose quantum efficiency is still rising at 600 nm.

28.2. Inorganic scintillators:

Revised September 2005 by C.L. Woody (BNL). and R.-Y. Zhu (California Inst. of Technology).

Inorganic crystals form a class of scintillating materials with much higher densities than organic plastic scintillators (typically $\sim 4\text{--}8\text{ g/cm}^3$) with a variety of different properties for use as scintillation detectors. Due to their high density and high effective atomic number, they can be used in applications where high stopping power or a high conversion efficiency for electrons or photons is required. These include total absorption electromagnetic calorimeters (see Sec. 28.12.1), which consist of a totally active absorber (as opposed to a sampling calorimeter), as well as serving as gamma ray detectors over a wide range of energies. Many of these crystals also have very high light output, and can therefore provide excellent energy resolution down to very low energies (\sim few hundred keV).

Some crystals are intrinsic scintillators in which the luminescence is produced by a part of the crystal lattice itself. However, other crystals require the addition of a dopant, typically fluorescent ions such as thallium (Tl) or cerium (Ce) which is responsible for producing the scintillation light. However, in both cases, the scintillation mechanism is the same. Energy is deposited in the crystal by ionization, either directly by charged particles, or by the conversion of photons into electrons or positrons which subsequently produce ionization. This energy is transferred to the luminescent centers which then radiate scintillation photons. The efficiency η for the conversion of energy deposit in the crystal to scintillation light can be expressed by the relation [28]

$$\eta = \beta \cdot S \cdot Q . \quad (28.1)$$

where β is the efficiency of the energy conversion process, S is the efficiency of energy transfer to the luminescent center, and Q is the quantum efficiency of the luminescent center. The value of η ranges between 0.1 and ~ 1 depending on the crystal, and is the main factor in determining the intrinsic light output of the scintillator. In addition, the scintillation decay time is primarily determined by the energy transfer and emission process. The decay time of the scintillator is mainly dominated by the decay time of the luminescent center. For example, in the case of thallium doped sodium iodide (NaI(Tl)), the value of η is ~ 0.5 , which results in a light output $\sim 40,000$ photons per MeV of

energy deposit. This high light output is largely due to the high quantum efficiency of the thallium ion ($Q \sim 1$), but the decay time is rather slow ($\tau \sim 250$ ns).

Table 28.2 lists the basic properties of some commonly used inorganic crystal scintillators. NaI(Tl) is one of the most common and widely used scintillators, with an emission that is well matched to a bialkali photomultiplier tube, but it is highly hygroscopic and difficult to work with, and has a rather low density. CsI(Tl) has high light yield, an emission that is well matched to solid state photodiodes, and is mechanically robust (high plasticity and resistance to cracking). However, it needs careful surface treatment and is slightly hygroscopic. Compared with CsI(Tl), pure CsI has identical mechanical properties, but faster emission at shorter wavelengths and light output approximately an order of magnitude lower. BaF₂ has a fast component with a sub-nanosecond decay time, and is the fastest known scintillator. However, it also has a slow component with a much longer decay time (~ 630 ns). Bismuth germanate (Bi₄Ge₃O₁₂ or BGO) has a very high density, and consequently a short radiation length X_0 and Molière radius R_M . BGO's emission is well-matched to the spectral sensitivity of photodiodes, and it is easy to handle and not hygroscopic. Lead tungstate (PbWO₄ or PWO) has a very high density, with a very short X_0 and R_M , but its intrinsic light yield is rather low. Both cerium doped lutetium oxyorthosilicate (Lu₂SiO₅:Ce, or LSO:Ce) [29] and cerium doped gadolinium orthosilicate (Gd₂SiO₅:Ce, or GSO:Ce) [30] are dense crystal scintillators which have a high light yield and a fast decay time.

Beside the crystals listed in Table 28.2, a number of new crystals are being developed that may have potential applications in high energy or nuclear physics. Of particular interest is the family of yttrium and lutetium perovskites, which include YAP (YAlO₃:Ce) and LuAP (LuAlO₃:Ce) and their mixed compositions. These have been shown to be linear over a large energy range [31], and have the potential for providing extremely good intrinsic energy resolution. In addition, other fluoride crystals such as CeF₃ have been shown to provide excellent energy resolution in calorimeter applications.

Table 28.2 gives the light output of other crystals relative to NaI(Tl) as measured with a bialkali photomultiplier tube. However, the useful signal produced by a scintillator is usually quoted in terms of the number of photoelectrons per MeV produced by a given photodetector. The relationship between the number of photons/MeV produced and photoelectrons/MeV detected involves the factors for the light collection efficiency L and the quantum efficiency QE of the photodetector:

$$N_{\text{p.e.}}/\text{MeV} = L \cdot QE \cdot N_{\gamma}/\text{MeV} \quad (28.2)$$

L includes the transmission of scintillation light within the crystal (*i.e.*, the bulk attenuation length of the material), reflections and scattering from the surfaces, and the size and shape of the crystal. These factors can vary considerably depending on the sample, but can be in the range of ~ 50 – 60% . However, the internal light transmission depends on the intrinsic properties of the material, as well as the number and type of impurities and defects that can produce internal absorption within the crystal, and can be highly affected by factors such as radiation damage, as discussed below.

The quantum efficiency depends on the type of photodetector used to detect the scintillation light, which is typically ~ 15 – 20% for photomultiplier tubes and $\sim 70\%$ for

8 28. Particle detectors

silicon photodiodes for visible wavelengths. The quantum efficiency of the detector is usually highly wavelength dependent, as shown in Fig. 28.2, and should be matched to the particular crystal of interest to give the highest quantum yield at the wavelength corresponding to the peak of the scintillation emission. The comparison of the light output given in Table 28.2 is for a standard photomultiplier tube with a bi-alkali photocathode. Results with different photodetectors can be significantly different. For example, the response of CsI(Tl) relative to NaI(Tl) with a silicon photodiode would be 140 rather than 45 due to its higher quantum efficiency at longer wavelengths. For scintillators which emit in the UV, a detector with a quartz window should be used.

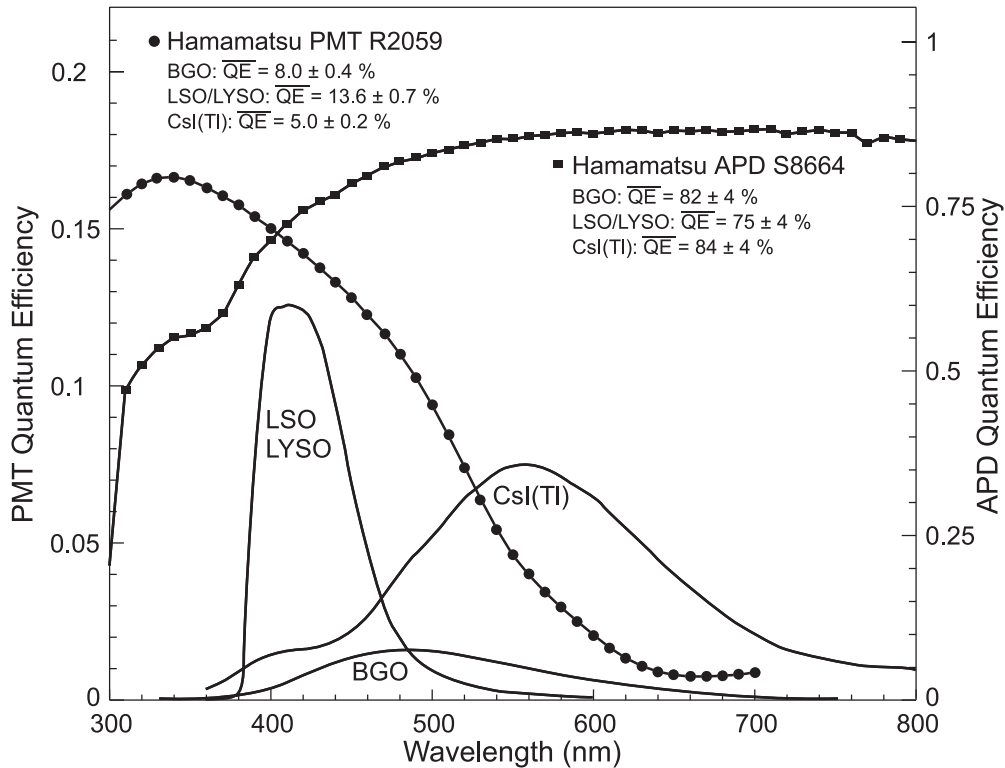


Figure 28.2: The quantum efficiencies of two photodetectors, a Hamamatsu R2059 PMT with bi-alkali cathode and a Hamamatsu S8664 avalanche photodiode (APD), are shown as a function of wavelength. Also shown in the figure are emission spectra of three crystal scintillators, BGO, LSO and CsI(Tl), and the numerical values of the emission weighted quantum efficiency. The area under each emission spectrum is proportional to crystal's light yield.

One important issue related to the application of a crystal scintillator is its radiation hardness. Stability of its light output, or the ability to track and monitor the variation of its light output in a radiation environment, is required for high resolution and precision calibration [32]. All known crystal scintillators suffer from radiation damage. A common damage phenomenon is the appearance of radiation induced absorption caused by the formation of impurities or point defect related color centers. This radiation induced absorption reduces the light attenuation length in the crystal, and

hence its light output. For crystals with high defect density, a severe reduction of light attenuation length may lead to a distortion of the light response uniformity, leading to a degradation of energy resolution. Additional radiation damage effects may include a reduced intrinsic scintillation light yield (damage to the luminescent centers) and an increased phosphorescence (afterglow). For crystals to be used in the construction a high precision calorimeter in a radiation environment, its scintillation mechanism must not be damaged and its light attenuation length in the expected radiation environment must be long enough so that its light response uniformity, and thus its energy resolution, does not change [33].

Most of the crystals listed in Table 28.2 have been used in high energy or nuclear physics experiments when the ultimate energy resolution for electrons and photons is desired. Examples are the Crystal Ball NaI(Tl) calorimeter at SPEAR, the L3 BGO calorimeter at LEP, the CLEO CsI(Tl) calorimeter at CESR, the KTeV CsI calorimeter at the Tevatron, and the BaBar and BELLE CsI(Tl) calorimeters at PEP-II and KEK. Because of its high density and low cost, PWO calorimeters are now being constructed by CMS and ALICE at LHC, by CLAS and PrimEx at CEBAF, and by BTeV at the Tevatron.

28.3. Cherenkov detectors

Written September 2003 by B.N. Ratcliff (SLAC).

Although devices using Cherenkov radiation are often thought of as particle identification (PID) detectors, in practice, they are widely used over a much broader range of applications; including (1) fast particle counters; (2) hadronic particle identification; and (3) tracking detectors performing complete event reconstruction. A few examples of specific applications from each category include; (1) the polarization detector of the SLD [34]; (2) the hadronic PID detectors at the B factory detectors (DIRC in BaBar [8] and the aerogel threshold Cherenkov in Belle [35]); and (3) large water Cherenkov counters such as Super-Kamiokande [36]. Cherenkov counters contain two main elements; (1) a radiator through which the charged particle passes, and (2) a photodetector. As Cherenkov radiation is a weak source of photons, light collection and detection must be as efficient as possible. The presence of the refractive index n and the path length of the particle in the radiator in the Cherenkov relations allows tuning these quantities for a particular experimental application.

Cherenkov detectors utilize one or more of the properties of Cherenkov radiation discussed in the Passages of Particles through Matter section (Sec. 27 of this *Review*): the prompt emission of a light pulse; the existence of a velocity threshold for radiation; and the dependence of the Cherenkov cone half-angle θ_c and the number of emitted photons on the velocity of the particle.

The number of photoelectrons ($N_{\text{p.e.}}$) detected in a given device is

$$N_{\text{p.e.}} = L \frac{\alpha^2 z^2}{r_e m_e c^2} \int \epsilon(E) \sin^2 \theta_c(E) dE , \quad (28.3)$$

where L is the path length in the radiator, $\epsilon(E)$ is the efficiency for collecting the Cherenkov light and transducing it in photoelectrons, and $\alpha^2/(r_e m_e c^2) = 370 \text{ cm}^{-1} \text{ eV}^{-1}$.

10 28. Particle detectors

Table 28.2: Properties of several inorganic crystal scintillators. Most of the notation is defined in Sec. 6 of this *Review*.

Parameter:	ρ	MP	X_0^*	R_M^*	dE/dx	λ_I^*	τ_{decay}	λ_{max}	n^{\natural}	Relative output [†]	Hygroscopic?	$d(\text{LY})/dT$
Units:	g/cm^3	$^{\circ}\text{C}$	cm	cm	MeV/cm	cm	ns	nm				$\%/^{\circ}\text{C}^{\ddagger}$
NaI(Tl)	3.67	651	2.59	4.13	4.8	42.9	230	410	1.85	100	yes	~ 0
BGO	7.13	1050	1.12	2.23	9.0	22.8	300	480	2.15	9	no	-1.6
BaF ₂	4.89	1280	2.03	3.10	6.6	30.7	630 ^s 0.9 ^f	300 ^s 220 ^f	1.50	21 ^s 2.7 ^f	no	-2 ^s $\sim 0^f$
CsI(Tl)	4.51	621	1.86	3.57	5.6	39.3	1300	560	1.79	45	slight	0.3
CsI(pure)	4.51	621	1.86	3.57	5.6	39.3	35 ^s 6 ^f	420 ^s 310 ^f	1.95	5.6 ^s 2.3 ^f	slight	-0.6
PbWO ₄	8.3	1123	0.89	2.00	10.2	20.7	50 ^s 10 ^f	560 ^s 420 ^f	2.20	0.1 ^s 0.6 ^f	no	-1.9
LSO(Ce)	7.40	2070	1.14	2.07	9.6	20.9	40	420	1.82	75	no	~ 0
GSO(Ce)	6.71	1950	1.38	2.23	8.9	22.2	600 ^s 56 ^f	430	1.85	3 ^s 30 ^f	no	-0.1

* Numerical values calculated using formulae in this review.

[‡] Refractive index at the wavelength of the emission maximum.

[†] Relative light yield measured with a bi-alkali cathode PMT.

[‡] Variation of light yield with temperature evaluated at room temperature.

f = fast component, *s* = slow component

The quantities ϵ and θ_c are functions of the photon energy E . However, since the typical energy dependent variation of the index of refraction is modest, a quantity called the *Cherenkov detector quality factor* N_0 can be defined as

$$N_0 = \frac{\alpha^2 z^2}{r_e m_e c^2} \int \epsilon dE, \quad (28.4)$$

so that

$$N_{\text{p.e.}} \approx LN_0 \langle \sin^2 \theta_c \rangle. \quad (28.5)$$

We take $z = 1$, the usual case in high-energy physics, in the following discussion.

This definition of the quality factor N_0 is not universal, nor, indeed, very useful for situations where the geometrical photon collection efficiency (ϵ_{coll}) varies substantially for different tracks. In this case, separate factors for photon collection and detection (ϵ_{det}), so that $\epsilon = \epsilon_{\text{coll}}\epsilon_{\text{det}}$, are sometimes included on the right hand side of the equation. A typical value of N_0 for a photomultiplier (PMT) detection system working in the visible and near UV, and collecting most of the Cherenkov light, is about 100 cm^{-1} . Practical

counters, utilizing a variety of different photodetectors, have values ranging between about 30 and 180 cm^{-1} . Radiators can be chosen from a variety of transparent materials (Sec. 27 of this *Review* and Table 6.1). In addition to refractive index, the choice requires consideration of factors such as material density, radiation length, transmission bandwidth, absorption length, chromatic dispersion, optical workability (for solids), availability, and cost. Long radiator lengths are required to obtain sufficient numbers of photons when the momenta of the particle species to be separated are high. Recently, the gap in refractive index that has traditionally existed between gases and liquid or solid materials has been partially closed with transparent *silica aerogels* with indices that range between about 1.007 and 1.13.

Cherenkov counters may be classified as either *imaging* or *threshold* types, depending on whether they do or do not make use of Cherenkov angle (θ_c) information. Imaging counters may be used to track particles as well as identify them.

28.3.1. Threshold counters: Threshold Cherenkov detectors [37], in their simplest form, make a yes/no decision based on whether the particle is above or below the Cherenkov threshold velocity $\beta_t = 1/n$. A straightforward enhancement of such detectors uses the number of observed photoelectrons (or a calibrated pulse height) to discriminate between species or to set probabilities for each particle species [38]. This strategy can increase the momentum range of particle separation by a modest amount (to a momentum some 20% above the threshold momentum of the heavier particle in a typical case).

Careful designs give $\langle \epsilon_{\text{coll}} \rangle \gtrsim 90\%$. For a photomultiplier with a typical bialkali cathode, $\int \epsilon_{\text{det}} dE \approx 0.27$, so that

$$N_{\text{p.e.}}/L \approx 90 \text{ cm}^{-1} \langle \sin^2 \theta_c \rangle \quad (\text{i.e., } N_0 = 90 \text{ cm}^{-1}). \quad (28.6)$$

Suppose, for example, that n is chosen so that the threshold for species a is p_t ; that is, at this momentum species a has velocity $\beta_a = 1/n$. A second, lighter, species b with the same momentum has velocity β_b , so $\cos \theta_c = \beta_a/\beta_b$, and

$$N_{\text{p.e.}} L \approx 90 \text{ cm}^{-1} \frac{m_a^2 - m_b^2}{p_t^2 + m_a^2}. \quad (28.7)$$

For K/π separation at $p = p_t = 1(5) \text{ GeV}/c$, $N_{\text{p.e.}}/L \approx 16(0.8) \text{ cm}^{-1}$ for π 's and (by design) 0 for K 's.

For limited path lengths $N_{\text{p.e.}}$ can be small, and a minimum number is required to trigger external electronics. The overall efficiency of the device is controlled by Poisson fluctuations, which can be especially critical for separation of species where one particle type is dominant. The effective number of photoelectrons is often less than the average number calculated above due to additional equivalent noise from the photodetector. It is common to design for at least 10 photoelectrons for the high velocity particle in order to obtain a robust counter. As rejection of the particle that is below threshold depends on *not* seeing a signal, electronic and other background noise can be important. Physics sources of light production for the below threshold particle, such as decay of the above threshold particle or the production of delta rays in the radiator, often limit the separation

12 28. Particle detectors

attainable, and need to be carefully considered. Well designed, modern multi-channel counters, such as the ACC at Belle [35], can attain good particle separation performance over a substantial momentum range for essentially the full solid angle of the spectrometer.

28.3.2. Imaging counters: The most powerful use of the information available from the Cherenkov process comes from measuring the ring-correlated angles of emission of the individual Cherenkov photons. Since low-energy photon detectors can measure only the position (and, perhaps, a precise detection time) of the individual Cherenkov photons (not the angles directly), the photons must be “imaged” onto a detector so that their angles can be derived [39]. In most cases the optics map the Cherenkov cone onto (a portion of) a distorted circle at the photodetector. Though this imaging process is directly analogous to the familiar imaging techniques used in telescopes and other optical instruments, there is a somewhat bewildering variety of methods used in a wide variety of counter types with different names. Some of the imaging methods used include (1) focusing by a lens; (2) proximity focusing (i.e., focusing by limiting the emission region of the radiation); and (3) focusing through an aperture (a pinhole). In addition, the prompt Cherenkov emission coupled with the speed of modern photon detectors allows the use of time imaging, a method which is used much less frequently in conventional imaging technology. Finally, full tracking (and event reconstruction) can be performed in large water counters by combining the individual space position and time of each photon together with the constraint that Cherenkov photons are emitted from each track at a constant polar angle.

In a simple model of an imaging PID counter, the fractional error on the particle velocity (δ_β) is given by

$$\delta_\beta = \frac{\sigma_\beta}{\beta} = \tan \theta_c \sigma(\theta_c) \quad , \quad (28.8)$$

where

$$\sigma(\theta_c) = \frac{\langle \sigma(\theta_i) \rangle}{\sqrt{N_{\text{p.e.}}}} \oplus C \quad , \quad (28.9)$$

where $\langle \sigma(\theta_i) \rangle$ is the average single photoelectron resolution, as defined by the optics, detector resolution and the intrinsic chromaticity spread of the radiator index of refraction averaged over the photon detection bandwidth. C combines a number of other contributions to resolution including, (1) correlated terms such as tracking, alignment, and multiple scattering, (2) hit ambiguities, (3) background hits from random sources, and (4) hits coming from other tracks. In many practical cases, the resolution is limited by these effects.

For a $\beta \approx 1$ particle of momentum (p) well above threshold entering a radiator with index of refraction (n), the number of σ separation (N_σ) between particles of mass m_1 and m_2 is approximately

$$N_\sigma \approx \frac{|m_1^2 - m_2^2|}{2p^2 \sigma(\theta_c) \sqrt{n^2 - 1}} \quad . \quad (28.10)$$

In practical counters, the angular resolution term $\sigma(\theta_c)$ varies between about 0.1 and 5 mrad depending on the size, radiator, and photodetector type of the particular counter. The range of momenta over which a particular counter can separate particle species

extends from the point at which the number of photons emitted becomes sufficient for the counter to operate efficiently as a threshold device ($\sim 20\%$ above the threshold for the lighter species) to the value in the imaging region given by the equation above. For example, for $\sigma(\theta_c) = 2\text{mrad}$, a fused silica radiator ($n = 1.474$), or a fluorocarbon gas radiator (C_5F_{12} , $n = 1.0017$), would separate π/K 's from the threshold region starting around $0.15(3)\text{ GeV}/c$ through the imaging region up to about $4.2(18)\text{ GeV}/c$ at better than 3σ .

Many different imaging counters have been built during the last several decades [42]. Among the earliest examples of this class of counters are the very limited acceptance Differential Cherenkov detectors, designed for particle selection in high momentum beam lines. These devices use optical focusing and/or geometrical masking to select particles having velocities in a specified region. With careful design, a velocity resolution of $\sigma_\beta/\beta \approx 10^{-4}$ – 10^{-5} can be obtained [37].

Practical multi-track Ring-Imaging Cherenkov detectors (generically called RICH counters) are a more recent development. They have been built in small-aperture and 4π geometries both as PID counters and as stand-alone detectors with complete tracking and event reconstruction as discussed more fully below. PID RICH counters are sometimes further classified by ‘generations’ that differ based on performance, design, and photodetection techniques.

A typical example of a first generation RICH used at the Z factory e^+e^- colliders [40,41] has both liquid (C_6F_{14} , $n = 1.276$) and gas (C_5F_{12} , $n = 1.0017$) radiators, the former being proximity imaged using the small radiator thickness while the latter use mirrors. The phototransducers are a TPC/wire-chamber combination having charge division or pads. They are made sensitive to photons by doping the TPC gas (usually, ethane/methane) with $\sim 0.05\%$ TMAE (tetrakis(dimethylamino)ethylene). Great attention to detail is required, (1) to avoid absorbing the UV photons to which TMAE is sensitive, (2) to avoid absorbing the single photoelectrons as they drift in the long TPC, and (3) to keep the chemically active TMAE vapor from interacting with materials in the system. In spite of their unforgiving operational characteristics, these counters attained good $e/\pi/K/p$ separation over wide momentum ranges during several years of operation. In particular, their π/K separation range extends over momenta from about 0.25 to $20\text{ GeV}/c$.

Second and third generation counters [42] generally must operate at much higher particle rates than the first generation detectors, and utilize different photon detection bandwidths, with higher readout channel counts, and faster, more forgiving photon detection technology than the TMAE doped TPCs just described. Radiator choices have broadened to include materials such as lithium fluoride, fused silica, and aerogel. Vacuum based photodetection systems (*e.g.*, photomultiplier tubes (PMT) or hybrid photodiodes (HPD)) have become increasingly common. They handle very high rates, can be used in either single or multi anode versions, and allow a wide choice of radiators. Other fast detection systems that use solid cesium iodide (CSI) photocathodes or triethylamine (TEA) doping in proportional chambers are useful with certain radiator types and geometries.

14 28. Particle detectors

A DIRC (Detector of Internally Reflected Cherenkov light) is a third generation subtype of a RICH first used in the BaBar detector [8]. It “inverts” the usual principle for use of light from the radiator of a RICH by collecting and imaging the total internally reflected light, rather than the transmitted light. A DIRC utilizes the optical material of the radiator in two ways, simultaneously; first as a Cherenkov radiator, and second, as a light pipe for the Cherenkov light trapped in the radiator by total internal reflection. The DIRC makes use of the fact that the magnitudes of angles are preserved during reflection from a flat surface. This fact, coupled with the high reflection coefficients of the total internal reflection process (> 0.9995 for highly polished SiO_2), and the long attenuation length for photons in high purity fused silica, allows the photons of the ring image to be transported to a detector outside the path of the particle where they may be imaged. The BaBar DIRC uses 144 fused silica radiator bars ($1.7 \times 3.5 \times 490$ cm) with the light being focused onto 11 000 conventional PMT’s located about 120 cm from the end of the bars by the “pinhole” of the bar end. DIRC performance can be understood using the formula for (N_σ) discussed above. Typically, $N_{\text{p.e.}}$ is rather large (between 15 and 60) and the Cherenkov polar angle is measured to about 2.5 mrad. The momentum range with good π/K separation extends up to about 4 GeV/ c , matching the B decay momentum spectrum observed in BaBar.

28.4. Cherenkov tracking calorimeters

Written August 2003 by D. Casper (UC Irvine).

In addition to the specialized applications described in the previous section, Cherenkov radiation is also exploited in large, ring-imaging detectors with masses measured in kilotons or greater. Such devices are not subdetector components, but complete experiments with triggering, tracking, vertexing, particle identification and calorimetric capabilities, where the large mass of the transparent dielectric medium serves as an active target for neutrino interactions (or their secondary muons) and rare processes like nucleon decay.

For volumes of this scale, absorption and scattering of Cherenkov light are non-negligible, and a wavelength-dependent factor $e^{-d/L(\lambda)}$ (where d is the distance from emission to the sensor and $L(\lambda)$ is the attenuation length of the medium) must be included in the integral of Eq. (28.3) for the photoelectron yield. The choice of medium is therefore constrained by the refractive index and transparency in the region of photodetector sensitivity; highly-purified water is an inexpensive and effective choice; sea-water, mineral oil, polar ice, and D_2O are also used. Photo-multiplier tubes (PMTs) on either a volume or surface lattice measure the time of arrival and intensity of Cherenkov radiation. Hemispherical PMTs are favored for the widest angular acceptance, and sometimes mounted with reflectors or wavelength-shifting plates to increase the effective photosensitive area. Gains and calibration curves are measured with pulsed laser signals transmitted to each PMT individually via optical fiber or applied to the detector as a whole through one or more diffusing balls.

Volume instrumentation [43] is only cost-effective at low densities, with a spacing comparable to the attenuation (absorption and scattering) length of Cherenkov light in the medium (15–40 m for Antarctic ice and ~ 45 m in the deep ocean). PMTs are

deployed in vertical strings as modular units which include pressure housings, front-end electronics and calibration hardware. The effective photocathode coverage of such arrays is less than 1% but still adequate (using timing information and the Cherenkov angular constraint) to reconstruct the direction of TeV muons to 1° or better. The size of such “neutrino telescopes” is limited only by cost once the technical challenges of deployment, power, signal extraction and calibration in an inaccessible and inhospitable environment are addressed; arrays up to $(1 \text{ km})^3$ in size are under study or development.

Surface instrumentation [44] allows the target volume to be viewed with higher photocathode density by a number of PMTs which scales like $(\text{volume})^{2/3}$. To improve hermeticity and shielding, and to ensure that an outward-going particle’s Cherenkov cone illuminates sufficient PMTs for reconstruction, a software-defined fiducial volume begins some distance ($\sim 2 \text{ m}$) inside the photosensor surface. Events originating within the fiducial volume are classified as *fully-contained* if no particles exit the inner detector, or *partially-contained* otherwise. An outer (veto) detector, optically separated from the inner volume and instrumented at reduced density, greatly assists in making this determination and also simplifies the selection of contained events. The maximum size of a pure surface array is limited by the attenuation length ($\sim 100 \text{ m}$ has been achieved for large volumes using reverse-osmosis water purification), pressure tolerance of the PMTs (< 80 meters of water, without pressure housings) and structural integrity of the enclosing cavity, if underground. In practice, these limitations can be overcome by a segmented design involving multiple modules of the nominal maximum size; megaton-scale devices are under study.

Cherenkov detectors are excellent electromagnetic calorimeters, and the number of Cherenkov photons *produced* by an e/γ is nearly proportional to its kinetic energy. For massive particles, the number of photons produced is also related to the energy, but not linearly. For any type of particle, the *visible energy* E_{vis} is defined as the energy of an electron which would produce the same number of Cherenkov photons. The number of photoelectrons *collected* depends on a detector-specific scale factor, with event-by-event corrections for geometry and attenuation. For typical PMTs, in water $N_{\text{p.e.}} \approx 15 \xi E_{\text{vis}}(\text{MeV})$, where ξ is the effective fractional photosensor coverage; for other materials, the photoelectron yield scales with the ratio of $\sin^2 \theta_c$ over density. At solar neutrino energies, the visible energy resolution ($\sim 30\%/\sqrt{\xi E_{\text{vis}}(\text{MeV})}$) is about 20% worse than photoelectron counting statistics would imply. For higher energies, multi-photoelectron hits are likely and the charge collected by each PMT (rather the number of PMTs firing) must be used; this degrades the energy resolution to approximately $2\%/\sqrt{\xi E_{\text{vis}}(\text{GeV})}$. In addition, the absolute energy scale must be determined with sources of known energy. Using an electron LINAC and/or nuclear sources, 0.5–1.5% has been achieved at solar neutrino energies; for higher energies, cosmic-ray muons, Michel electrons and π^0 from neutrino interactions allow $\sim 3\%$ absolute energy calibration.

A trigger can be formed by the coincidence of PMTs within a window comparable to the detector’s light crossing time; the coincidence level thus corresponds to a visible energy threshold. Physics analysis is usually not limited by the hardware trigger, but rather the ability to reconstruct events. The interaction vertex can be estimated using timing and refined by applying the Cherenkov angle constraint to identified ring edges. Multi-ring

16 28. Particle detectors

events are more strongly constrained, and their vertex resolution is 33–50% better than single rings. Vertex resolution depends on the photosensor density and detector size, with smaller detectors performing somewhat better than large ones (~ 25 cm is typical for existing devices). Angular resolution is limited by multiple scattering at solar neutrino energies (25–30°) and improves to a few degrees around $E_{vis} = 1$ GeV.

A non-showering (μ, π^\pm, p) track produces a sharp ring with small contributions from delta rays and other radiated secondaries, while the more diffuse pattern of a showering (e, γ) particle is actually the superposition of many individual rings from charged shower products. Using maximum likelihood techniques and the Cherenkov angle constraint, these two topologies can be distinguished with an efficiency which depends on the photosensor density and detector size [45]. This particle identification capability has been confirmed by using cosmic-rays and Michel electrons, as well as charged-particle [46] and neutrino [47] beams. Large detectors perform somewhat better than smaller ones with identical photocathode coverage; a misidentification probability of $\sim 0.4\%/ \xi$ in the sub-GeV range is consistent with the performance of several experiments for $4\% < \xi < 40\%$. Detection of a delayed coincidence from muon decay offers another, more indirect, means of particle identification; with suitable electronics, efficiency approaches 100% for μ^+ decays but is limited by nuclear absorption (22% probability in water) for μ^- .

Reconstruction of multiple Cherenkov rings presents a challenging pattern recognition problem, which must be attacked by some combination of heuristics, maximum likelihood fitting, Hough transforms and/or neural networks. The problem itself is somewhat ill-defined since, as noted, even a single showering primary produces many closely-overlapping rings. For $\pi^0 \rightarrow \gamma\gamma$ two-ring identification, performance falls off rapidly with increasing π^0 momentum, and selection criteria must be optimized with respect to the analysis-dependent cost-function for $e \leftrightarrow \pi^0$ mis-identification. Two representative cases for $\xi = 39\%$ will be illustrated. In an atmospheric neutrino experiment, where π^0 are relatively rare compared to e^\pm , one can isolate a $> 90\%$ pure 500 MeV/c π^0 sample with an efficiency of $\sim 40\%$. In a ν_e appearance experiment at $E_\nu \leq 1$ GeV, where e^\pm are rare compared to π^0 , a 99% pure 500 MeV/c electron sample can be identified with an efficiency of $\sim 70\%$. For constant ξ , a larger detector (with, perforce, a greater number of pixels to sample the light distribution) performs somewhat better at multi-ring separation than a smaller one. For a more detailed discussion of event reconstruction techniques, see Ref. 36.

28.5. Transition radiation detectors (TRD's)

Revised September 2003 by D. Froidevaux (CERN).

It is clear from the discussion in the section on “Passages of Particles Through Matter” (Sec. 27 of this *Review*) that transition radiation (TR) only becomes useful for particle detectors when the signal can be observed as x rays emitted along the particle direction for Lorentz factors γ larger than 1000. In practice, TRD's are therefore used to provide

Table 28.3: Properties of Cherenkov tracking calorimeters. LSND was a hybrid scintillation/Cherenkov detector; the estimated ratio of isotropic to Cherenkov photoelectrons was about 5:1. MiniBooNE’s light yield also includes a small scintillation component.

Detector	Fiducial mass (kton)	PMTs (diameter, cm)	ξ	p.e./ MeV	Dates
IMB-1 [48]	3.3 H ₂ O	2048 (12.5)	1%	0.25	1982–85
IMB-3 [49]	3.3 H ₂ O	2048 (20 +plate)	4.5%	1.1	1987–90
KAM I [50,51]	0.88/0.78 H ₂ O	1000/948 (50)	20%	3.4	1983–85
KAM II [52]	1.04 H ₂ O	948 (50)	20%	3.4	1986–90
LSND [53]	0.084 oil+scint.	1220 (20)	25%	33	1993–98
SK-1 [54]	22.5 H ₂ O	11146 (50)	39%	6	1997–2001
SK-2	22.5 H ₂ O	5182 (50)	18%	3	2002–
K2K [55]	0.025 H ₂ O	680 (50)	39%	6	1999–
SNO [56]	1.0 D ₂ O	9456 (20+cone)	55%	9	1999–
MiniBooNE	0.445 oil	1280 (20)	10%	3–4	2002–

electron/pion separation for $0.5 \text{ GeV}/c \lesssim p \lesssim 100 \text{ GeV}/c$. The charged-particle momenta have usually been measured elsewhere in the detector in the past [57].

Since soft x rays, in the useful energy range between 2 and 20 keV, are radiated with about 1% probability per boundary crossing, practical detectors use radiators with several hundred interfaces, *e.g.* foils or fibers of low- Z materials such as polypropylene (or, more rarely, lithium) in a gas. Absorption inside the radiator itself and in the inactive material of the x-ray detector is important and limits the usefulness of the softer x rays, but interference effects are even larger, and saturate the x-ray yield for electron energies above a few GeV [58,59].

A classical detector is composed of several similar modules, each consisting of a radiator and an x-ray detector, which is usually a wire chamber operated with a xenon-rich mixture, in order to efficiently absorb the x rays. The most prominent and recent examples of such detectors for large-scale experiments are the TRD detectors of NOMAD [60], ALICE [61], and PHENIX. Since transition-radiation photons are mostly emitted at very small angles with respect to the charged-particle direction, the x-ray detector most often detects the sum of the ionization loss (dE/dx) of the charged particle in the gas and energy deposition of the x rays. The discrimination between electrons and pions can be based on the charges measured in each detection module, on the number of energy clusters observed above an optimal threshold (usually in the 5 to 7 keV region), or on more sophisticated methods analyzing the pulse shape as a function of time. Once properly calibrated and optimized, most of these methods yield very similar results.

Development work over the past years for accelerator (ATLAS [62]) and space (AMS [63], PAMELA [64]) applications has aimed at increasing the intrinsic quality of the TRD-performance by increasing the probability per detection module of observing a

18 28. Particle detectors

signal from TR-photons produced by electrons. This has been achieved experimentally by distributing small-diameter straw-tube detectors uniformly throughout the radiator material. This method has thereby also cured one of the major drawbacks of more classical TRD's, that is, their need to rely on another detector to measure the charged-particle trajectory. For example, in the ATLAS Transition Radiator Tracker [65] charged particles cross about 35 straw tubes embedded in the radiator material. Dedicated R&D work and detailed simulations have shown that the combination of charged-track measurement and particle identification in the same detector will provide a very powerful tool even at the highest LHC luminosity [66].

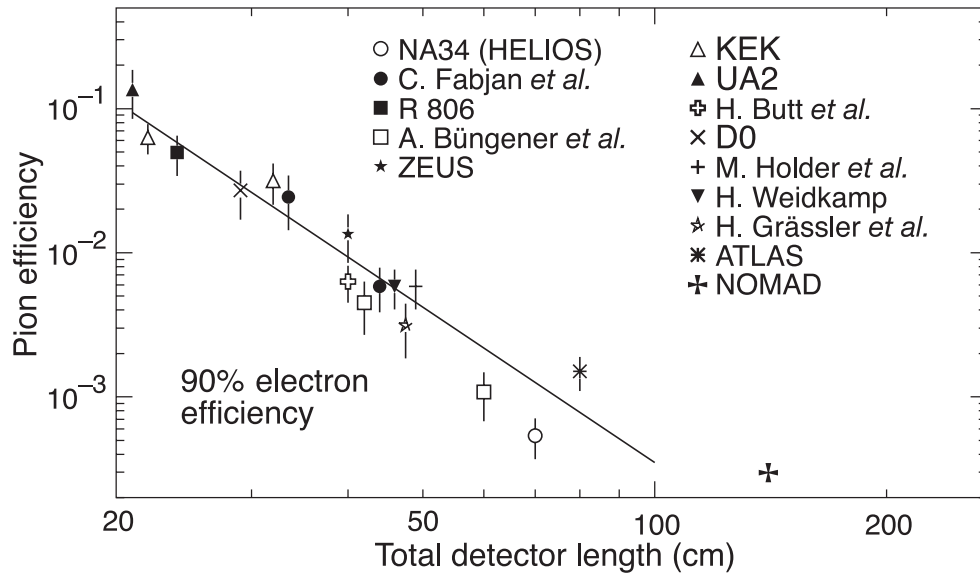


Figure 28.3: Pion efficiency measured (or predicted) for different TRDs as a function of the detector length for a fixed electron efficiency of 90%. The experimental data are directly taken or extrapolated from references [67–79,60](NA34 to NOMAD).

The major factor in the performance of any TRD is its overall length. This is illustrated in Fig. 28.3, which shows, for a variety of detectors, the measured (or predicted) pion efficiency at a fixed electron efficiency of 90% as a function of the overall detector length. The experimental data cover too wide a range of particle energies (from a few GeV to 40 GeV) to allow for a quantitative fit to a universal curve. Fig. 28.3 shows that an order of magnitude in rejection power against pions is gained each time the detector length is increased by ~ 20 cm.

28.6. Wire chambers

Written October 1999 by A. Cattai and G. Rolandi (CERN).

A wire chamber relies on the detection of a large fraction of the charge created in a volume filled with an appropriate gas mixture. A charged particle traversing a gas layer of thickness Δ produces electron-ion pairs along its path (see Sec. 27.2). The yield ($1/\lambda$) of ionization encounters for a minimum ionization particle (m.i.p.) (see Fig. 27.1) is given in Table 28.4.

Table 28.4: For various gases at STP: (a) yield of ionization encounters ($1/\lambda$) for m.i.p. [80], (b) t_{99} : thickness of the gas layer for 99% efficiency, and (c) the average number of free electrons produced by a m.i.p. (calculated using data from Ref. 81).

	Encounters/cm	t_{99} (mm)	Free electrons/cm
He	5	9.2	16
Ne	12	3.8	42
Ar	25	1.8	103
Xe	46	1.0	340
CH ₄	27	1.7	62
CO ₂	35	1.3	107
C ₂ H ₆	43	1.1	113

The probability to have at least one ionization encounter is $1 - \exp(-\Delta/\lambda)$ and the thickness of the gas layer for 99% efficiency is $t_{99} = 4.6\lambda$. Depending on the gas, some 65–80% of the encounters result in the production of only one electron; the probability that a cluster has more than five electrons is smaller than 10%. However the tail of the distribution is very long and the yield of ionization electrons is 3–4 times that of the ionization encounters. The secondary ionization happens either in collisions of (primary) ionization electrons with atoms or through intermediate excited states. The process is non-linear and gas mixtures may have larger yields than each of their components. See also the discussion in Sec. 27.7.

Under the influence of electric and magnetic fields the ionization electrons drift inside the gas with velocity \mathbf{u} given by:

$$\mathbf{u} = \mu|\mathbf{E}|\frac{1}{1 + \omega^2\tau^2} \left(\hat{\mathbf{E}} + \omega\tau(\hat{\mathbf{E}} \times \hat{\mathbf{B}}) + \omega^2\tau^2(\hat{\mathbf{E}} \cdot \hat{\mathbf{B}})\hat{\mathbf{B}} \right) \quad (28.11)$$

where $\hat{\mathbf{E}}$ and $\hat{\mathbf{B}}$ are unit vectors in the directions of the electric and magnetic fields respectively, μ is the electron mobility in the gas, ω is the cyclotron frequency eB/mc , and $\tau = \mu m/e$ is the mean time between collisions of the drifting electrons. The magnitude of the drift velocity depends on many parameters; typical values are in the range 1–8 cm/ μ s.

In a quite common geometry, the drift electric field is perpendicular to the magnetic field. In this case the electrons drift at an angle ψ with respect to the electric field direction such that $\tan\psi = \omega\tau$.

20 28. Particle detectors

The ionization electrons are eventually collected by a thin (typically 10 μm radius) anode wire where a strong electric field—increasing as $1/r$ —accelerates the electrons enough to produce secondary ionization and hence an avalanche. A quenching gas (organic molecules with large photo-absorption cross-section) absorbs the majority of the photons produced during the avalanche development, keeping the avalanche region localized. The gain achievable with a wire counter depends exponentially on the charge density on the wire, on the gas density ρ and—through it—on pressure and temperature: $dG/G \approx -Kd\rho/\rho$, where the coefficient K ranges between 5 and 8 in practical cases. Gains larger than 10^4 can be obtained in proportional mode.

The electrons produced in the avalanche are collected by the wire in a few nanoseconds. The positive ions move away from the wire and generate a signal that can be detected with an amplifier. Depending on whether the wire is treated as a current source or a voltage source, the signal is described respectively by:

$$I(t) = q \frac{d}{dt} F(t) ; \quad \Delta V(t) = \frac{q}{C} F(t) , \quad (28.12)$$

where q is the positive charge in the avalanche, C is the capacitance between the anode wire and the cathodes and $F(t) = \ln(1 + t/t_0) / \ln(1 + t_{\text{max}}/t_0)$. The constant t_0 is of the order of one or few nanoseconds; the constant t_{max} (several microseconds) describes the time that it takes ions to reach the cathodes.

A sketch of the first multi-wire proportional chamber (MWPC) [82] is shown in Fig. 28.4. It consists of a plane of parallel sense wires with spacing s and length L inserted in a gap of thickness Δ . The potential distributions and fields in a proportional or drift chamber can usually be calculated with good accuracy from the exact formula for the potential around an array of parallel line charges q (coul/m) along z and located at $y = 0, x = 0, \pm s, \pm 2s, \dots$,

$$V(x, y) = -\frac{q}{4\pi\epsilon_0} \ln \left\{ 4 \left[\sin^2 \left(\frac{\pi x}{s} \right) + \sinh^2 \left(\frac{\pi y}{s} \right) \right] \right\} . \quad (28.13)$$

With digital readout, the resolution in the direction perpendicular to the wire is $s/\sqrt{12}$, where s is typically 1–2 mm. Similar resolution can be achieved with a smaller channel density by measuring the difference in time between the arrival of electrons at the wire and the traversal of the particle, albeit with a longer response time. In the case of drift chambers, the spatial resolution is limited by the diffusion of ionization electrons during the drift and by the fluctuations of the ionization process. Depending on the gas mixture, the width of the diffusing cloud after 1 cm of drift is typically between 50 and 300 μm ; small diffusion implies low drift velocity. With drift lengths up to 5 cm (1 μs), resolutions in the range 100–200 μm have been achieved in chambers with surface areas of several square meters [84]. The central detectors in many collider experiments are drift chambers with the wires parallel to the beam direction. Small volume chambers (0.1 m^3) have been used for vertex measurement achieving resolutions of 50 μm using high pressure (2–4 bar) and low diffusion gas mixtures [85]. Large volume chambers (5–40 m^3) with several thousand wires of length of 1–2 meters are operated with resolution between 100 and 200 μm [86].

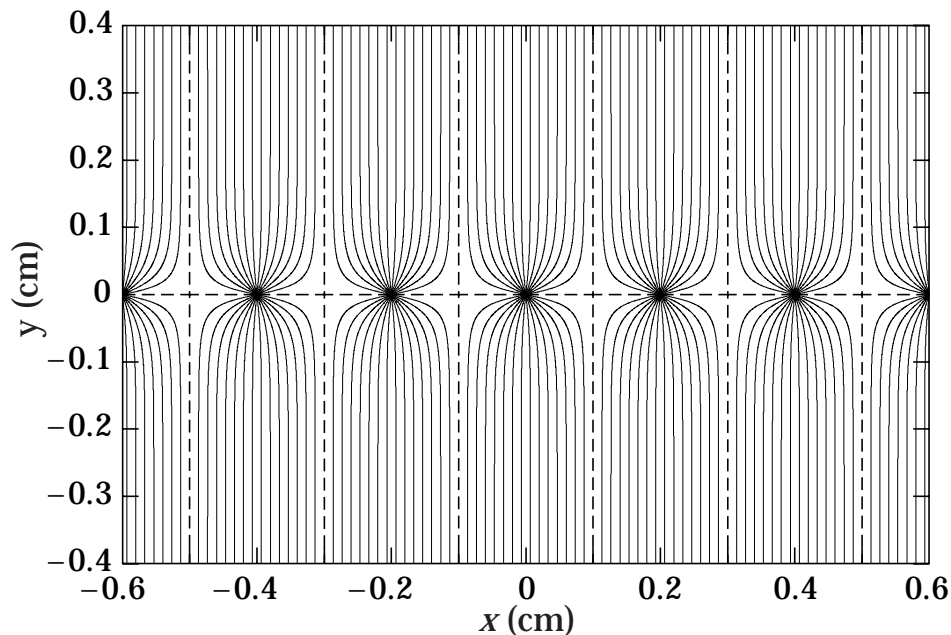


Figure 28.4: Electric field lines in a (MWPC) with an anode pitch of 2 mm as calculated with GARFIELD program [83].

The spatial resolution cannot be improved by arbitrarily reducing the spacing of the wires. In addition to the practical difficulties of precisely stringing wires at a pitch below 1 mm, there is a fundamental limitation: the electrostatic force between the wires is balanced by the mechanical tension, which cannot exceed a critical value. This gives the following approximate stability condition:

$$\frac{s}{L} \geq 1.5 \times 10^{-3} V(\text{kV}) \sqrt{\frac{20 \text{ g}}{T}}, \quad (28.14)$$

where V is the voltage of the sense wire and T is the tension of the wire in grams-weight equivalent.

A review of the principle of particle detection with drift chambers can be found in [87]. A compilation of the mobilities, diffusion coefficients and drift deflection angles as a function of \mathbf{E} and \mathbf{B} for several gas mixtures used in proportional chambers can be found in [88]. A review of micro-strip gas chambers (MSGC) can be found in [89].

28.7. Micro-pattern Gas Detectors

Written October 2005 by M.T Ronan (LBNL).

New micro-pattern gas detectors (MPGD's) are replacing conventional wire chambers in many applications. In these devices electron gas amplification is obtained in very high fields generated by modest voltages (300–400 V) across 50–100 μm structures suitable for large-area applications. Typically gains of 10^3 to 10^4 are achieved with many gases under standard conditions. Two examples of MPGD's are gas electron multipliers (GEM's) [98] and Micromegas [99].

22 28. Particle detectors

A GEM detector is typically fabricated by etching $50\ \mu\text{m}$ holes at a $140\ \mu\text{m}$ pitch in a thin ($50\ \mu\text{m}$) metal-clad sheet of insulating material. A potential difference is maintained between opposite sides of the sheet, so that electron avalanches occur in the holes. Electrons more or less follow the field lines as shown in Fig. 28.5.

A Micromegas structure is made by separating a thin ($5\ \mu\text{m}$) metallic mesh with $50\ \mu\text{m}$ pitch holes from a conducting or resistive anode plane using small $50\text{--}100\ \mu\text{m}$ -tall spacers. Electron and positive ion drift lines are shown in Fig. 28.6.

Fast electron and ion signals with risetimes of a few nsec and full widths of $20\text{--}100$ nsec, respectively, are obtained from direct charge collection with no loss due to ballistic deficit effects or the $1/t$ tails present in wire chambers. Positive ion feedback is determined by the ratio of drift and amplification fields, and by transfer fields in the case of multilayer GEM configurations. Typical drift or conversion fields of $100\text{--}1000\ \text{V/cm}$ and amplification fields of $40\text{--}70\ \text{kV/cm}$ leads to intrinsic feedback suppression of a few to several parts per mil.

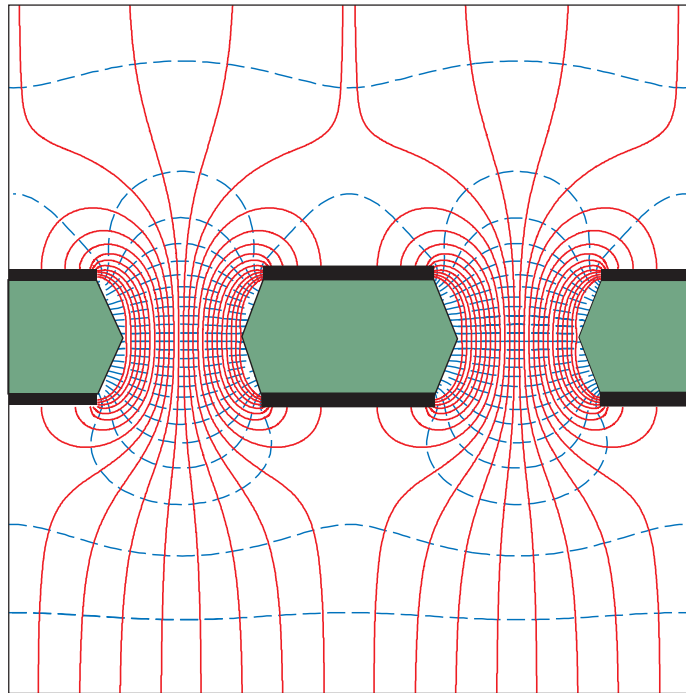


Figure 28.5: Detail of electric field lines (solid) and equipotentials (dashed) in the region of GEM holes. Electron transparencies are typically 100%. Most positive ions produced in the high field region within a hole drift back to the GEM's top side. Figure courtesy of F. Sauli.

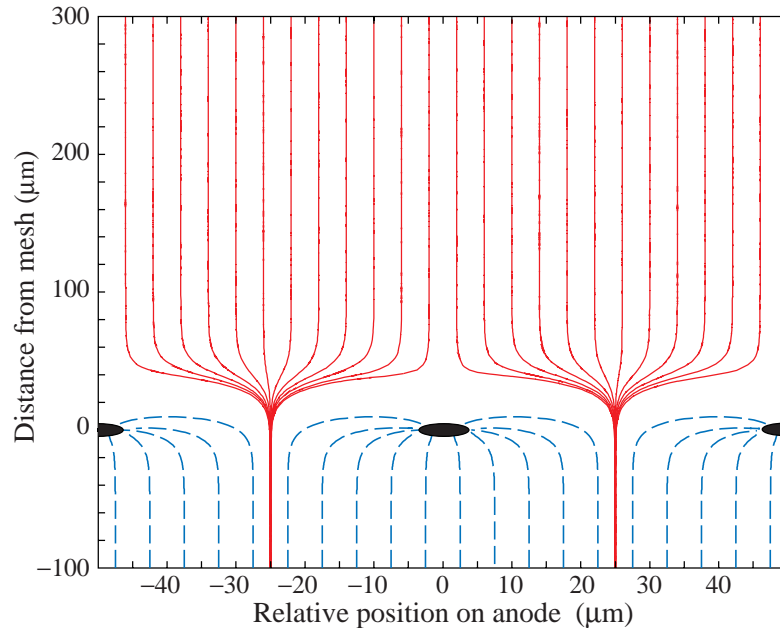


Figure 28.6: GARFIELD simulation of the electron (solid) and positive ion (dashed) drift lines in a Micromegas avalanche region. Drifting electrons are funneled through the mesh and spread across the anode surface by diffusion (not included). Most positive ions produced in the gap near the anode surface drift back to the Micromegas mesh.

28.8. Resistive-plate chambers

Written November 2005 by H.R. Band (U. Wisconsin) and J. Zhang (Beijing).

The resistive-plate chamber (RPC) was developed by Santonico and Cardarelli in the early 1980's [92] as a low-cost alternative to large scintillator planes.* Most commonly, an RPC is constructed from two parallel high-resistivity (10^9 – 10^{13} Ω -cm) glass or phenolic (Bakelite)/melamine laminate plates with a few-mm gap between them which is filled with atmospheric-pressure gas. The gas is chosen to absorb UV photons in order to limit transverse growth of discharges. The backs of the plates are coated with a lower-resistivity paint or ink ($\sim 10^5$ Ω/\square), and a high potential (7–12 keV) is maintained between them. The passage of a charged particle initiates an electric discharge, whose size and duration are limited since the current reduces the local potential to below that needed to maintain the discharge. The sensitivity of the detector outside of this region is unaffected. The signal readout is via capacitive coupling to metallic strips on both sides of the detector which are separated from the high voltage coatings by thin insulating sheets. The x and y position of the discharge can be measured if the strips on opposite sides of the gap are orthogonal. When operated in streamer mode, the induced signals on the strips can be quite large (~ 300 mV), making sensitive electronics unnecessary. An example of an RPC structure is shown in Fig. 28.7.

* It was based on earlier work on a spark counter with one high-resistivity plate [93].

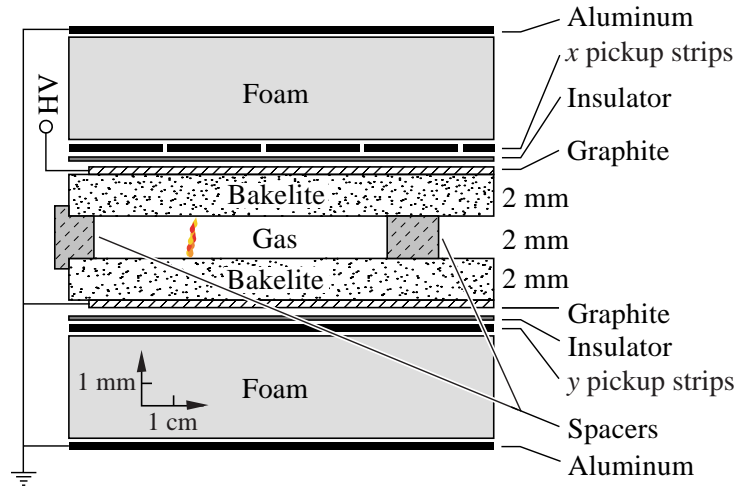


Figure 28.7: Schematic cross section of a typical RPC, in this case the single-gap streamer-mode BaBar RPC.

RPC's have inherent rate limitations since the time needed to re-establish the field after a discharge is proportional to the chamber capacitance and plate resistance. The average charge per streamer is 100–1000 pC. Typically, the efficiency of streamer-mode glass RPC's begins to fall above ~ 0.4 Hz/cm². Because of Bakelite's lower bulk resistivity, Bakelite RPC's can be efficient at 10–100 Hz/cm². The need for higher rate capability led to the development of avalanche-mode RPC's, in which the gas and high voltage have been tuned to limit the growth of the electric discharge, preventing streamer formation. Typical avalanche-mode RPC's have a signal charge of about 10 pC and can be efficient at 1 kHz/cm². The avalanche discharge produces a much smaller induced signal on the pickup strips (~ 1 mV) than streamers, and thus requires a more sophisticated and careful electronic design.

Many variations of the initial RPC design have been built for operation in either mode. Efficiencies of $\gtrsim 92\%$ for single gaps can be improved by the use of two or more gas gaps with shared pickup strips. Non-flammable and more environmentally friendly gas mixtures have been developed. In streamer mode, various mixtures of argon with isobutane and tetrafluoroethane have been used. For avalanche mode operation, a gas mixture of tetrafluoroethane (C₂H₂F₄) with 2–5% isobutane and 0.4–10% sulphur hexafluoride (SF₆) is typical. An example of large-scale RPC use is provided by the muon system being built for the ATLAS detector, where three layers of pairs of RPC's are used to trigger the drift tube arrays between the pairs. The total area is about 10,000 m². These RPC's provide a spatial resolution of 1 cm and a time resolution of 1 ns at an efficiency $\geq 99\%$. Much better timing resolution (50 ps) has been obtained using thin multiple-gap RPC's. Fonte provides useful review [94] of RPC designs.

Operational experience with RPC's has been mixed. Several experiments (*e.g.*, L3 and HARP) have reported reliable performance. However, the severe problems experienced with the BaBar RPC's have raised concerns about the long-term reliability of Bakelite RPC's.

Glass RPC's have had fewer problems, as seen by the history of the BELLE chambers. A rapid growth in the noise rate and leakage current in some of the BELLE glass RPC's was observed during commissioning. It was found that water vapor in the input gas was reacting with fluorine (produced by the disassociation of the tetrafluoroethane in the streamers) to produce hydrofluoric acid. The acid etched the glass surfaces, leading to increased noise rates and lower efficiencies. The use of copper gas piping to insure the dryness of the input gas stopped the problem. The BELLE RPC's have now operated reliably for more than 5 years. Even so, high noise rates in the outermost endcap layers have significantly reduced efficiencies there.

Several different failure modes diagnosed in the first-generation BaBar Bakelite RPC's caused the average efficiency of the barrel RPC's to fall from $\gtrsim 90\%$ to 35% in five years. The linseed oil which is used in Bakelite RPC's to coat the inner surface [95] had not been completely cured. Under warm conditions (32° C) and high voltage, oil collected on the spacers between the gaps or formed oil-drop bridges between the gaps. This led to large leakage currents (50–100 μA in some chambers) which persisted even when the temperature was regulated at 20° C. In addition, the graphite layer used to distribute the high voltage over the Bakelite became highly resistive (100 $\text{k}\Omega/\square \rightarrow 10 \text{M}\Omega/\square$), resulting in lowered efficiency in some regions and the complete death of whole chambers.

The BaBar problems and the proposed use of Bakelite RPC's in the LHC detectors prompted detailed studies of RPC aging and have led to improved construction techniques and a better understanding of RPC operational limits. The graphite layer has been improved and should be stable with integrated currents of $\lesssim 600 \text{mC}/\text{cm}^2$. Molded gas inlets and improved cleanliness during construction have reduced the noise rate of new chambers. Unlike glass RPC's, Bakelite RPC's have been found to require humid input gases to prevent drying of the Bakelite (increasing the bulk resistivity) which would decrease the rate capability. Second-generation BaBar RPC's incorporating many of the above improvements have performed reliably for over two years [96].

With many of these problems solved, new-generation RPC's are now being or soon will be used in about a dozen cosmic-ray and HEP detectors. Their comparatively low cost, ease of construction, good time resolution, high efficiency, and moderate spatial resolution make them attractive in many situations, particularly those requiring fast timing and/or large-area coverage.

28.9. Time-projection chambers

Revised August 2005 by M.T Ronan (LBNL).

Detectors with long drift distances perpendicular to a readout pad plane provide three-dimensional information, with one being the time projection. A (typically strong) magnetic field parallel to the drift direction suppresses transverse diffusion ($\sigma = \sqrt{2Dt}$) by a factor

$$D(B)/D(0) = \frac{1}{1 + \omega^2\tau^2} , \quad (28.15)$$

where D is the diffusion coefficient, $\omega = eB/mc$ is the cyclotron frequency, and τ is the mean time between collisions. Multiple measurements of energy deposit along the particle

trajectory combined with the measurement of momentum in the magnetic field allows excellent particle identification [97], as can be seen in Fig. 28.8.

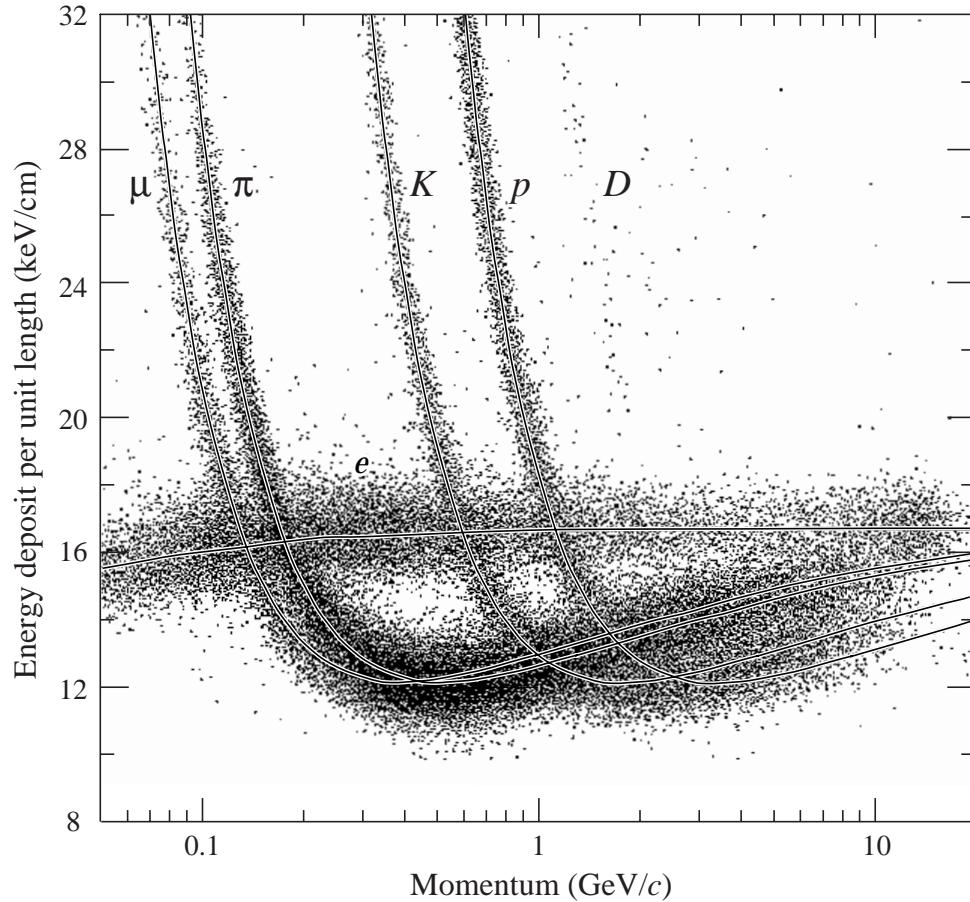


Figure 28.8: PEP4/9-TPC energy-deposit measurements (185 samples @8.5 atm Ar-CH₄ 80–20%) in multihadron events. The electrons reach a Fermi plateau value of 1.4 times the most probably energy deposit at minimum ionization. Muons from pion decays are separated from pions at low momentum; π/K are separated over all momenta except in the cross-over region. (Low-momentum protons and deuterons originate from hadron-nucleus collisions in inner materials such as the beam pipe.)

A typical gas-filled TPC consists of a long uniform drift region (1–2 m) generated by a central high-voltage membrane and precision concentric cylindrical field cages within a uniform, parallel magnetic field [87]. A multiwire proportional plane, Gas Electron Multiplier (GEM) [98] or Micromegas [99] micropattern device provides primary electron gas amplification. Details of construction and electron trajectories for a multiwire proportional anode plane are shown in Fig. 28.9. Signal shaping and processing using analog storage devices or FADC's allows excellent pattern recognition, track reconstruction, and particle identification within the same detector.

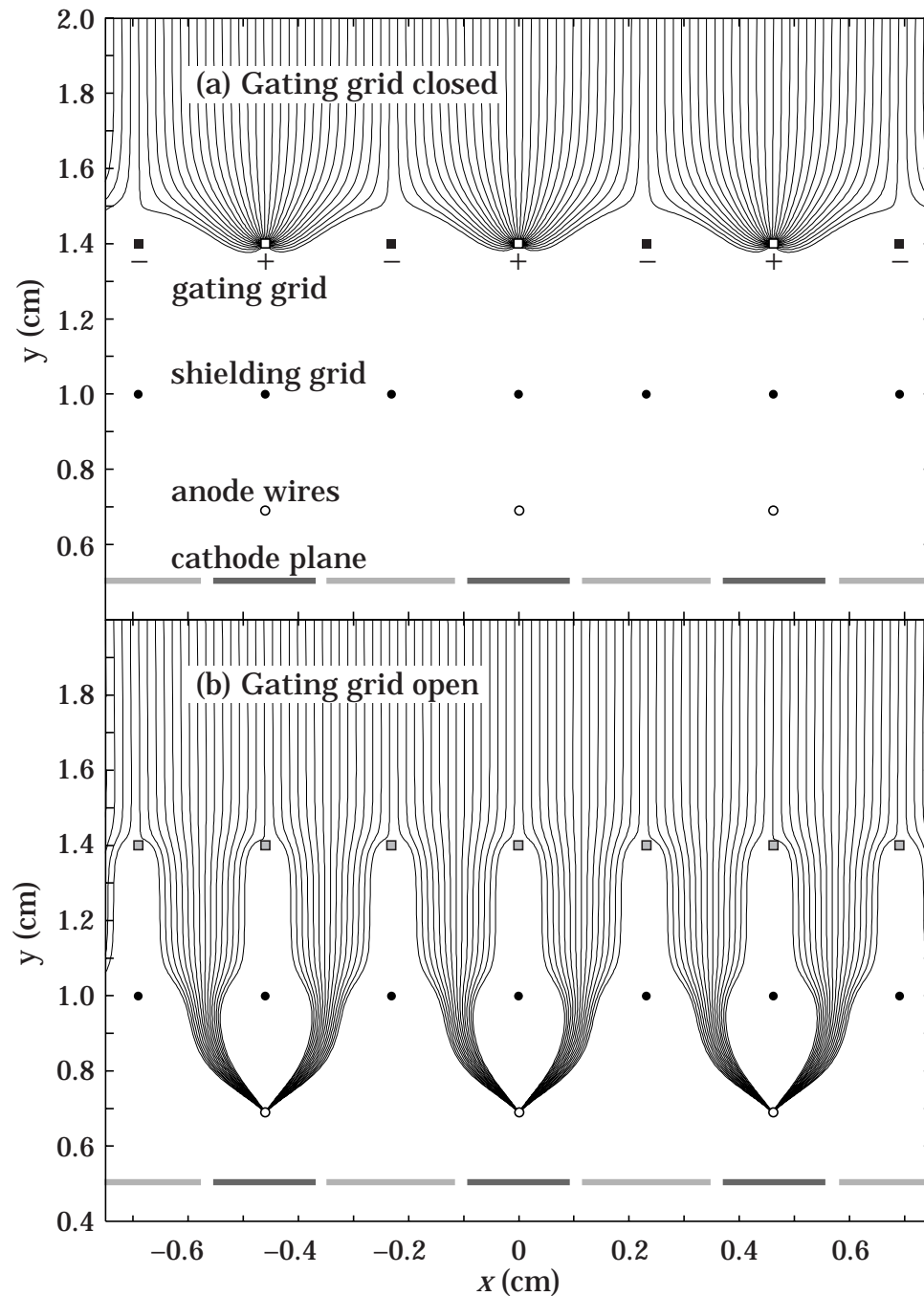


Figure 28.9: (a) Drifting electrons are collected on the gating grid until gated open by a triggering event. A shielding grid at ground potential is used to terminate the drift region. Electrons drifting through an open gating grid (b) pass through to the amplification region around the anode wires. Positive ions generated in the avalanche are detected on segmented cathode pads to provide precise measurements along the wire. The slow positive ions are blocked from entering the drift region by closing the gating grid after the electrons have drifted through.

28 28. Particle detectors

Typical values:

Gas: Ar + (10–20%) CH ₄	Pressure(P) = 1–8.5 atm.
$E/P = 100\text{--}200$ V/cm/atm	$B = 1\text{--}2$ Tesla
$v_{\text{drift}} = 5\text{--}7$ cm/ μ s	$\omega\tau = 1\text{--}8$
$\sigma_{x \text{ or } y} = 100\text{--}200$ μ m	$\sigma_z = 0.2\text{--}1$ mm
$\sigma_{E \text{ dep}} = 2.5\text{--}5.5$ %	

Truncated mean energy-deposit resolution depends on the number and size of samples, and gas pressure:

$$\sigma_{E \text{ dep}} \propto N^{-0.43} \times (P\ell)^{-0.32} . \quad (28.16)$$

Here N is the number of samples, ℓ is the sample size, and P is the pressure. Typical energy-deposit distributions are shown in Fig. 28.8. Good three-dimensional two-track resolutions of about 1–1.5 cm are routinely achieved.

$E \times B$ distortions arise from nonparallel E and B fields (see Eq. (28.11)), and from the curved drift of electrons to the anode wires in the amplification region of MWPC's. Much higher pitch MPGD readout eliminates the latter distortion and reduces signal spread on the pad plane. Position measurement errors include contributions from the anode-cathode geometry, the track crossing angle (α), $E \times B$ distortions, and from the drift diffusion of electrons

$$\sigma_{x \text{ or } y}^2 = \sigma_0^2 + \sigma_D^2(1 + \tan^2 \alpha)L/L_{\text{max}} + \sigma_\alpha^2(\tan \alpha - \tan \psi)^2 \quad (28.17)$$

where σ is the coordinate resolution, σ_0 includes the anode-cathode geometry contribution, ψ is the Lorentz angle, and L is the drift distance.

Space-charge distortions arise in high-rate environments, especially for low values of $\omega\tau$. However, they are mitigated by an effective gating grid (Fig. 28.9). Field uniformities of

$$\int (E_\perp/E) dz \lesssim 0.5\text{--}1 \text{ mm} , \quad (28.18)$$

over 10–40 m³ volumes have been obtained. Laser tracks and calibration events allow mapping of any remnant drift non-uniformities.

28.10. Silicon semiconductor detectors

Updated September 2005 by H. Spieler (LBNL).

Semiconductor detectors are widely used in modern high-energy physics experiments. They are the key ingredient of high-resolution vertex and tracking detectors and are also used as photodetectors in scintillation calorimeters. The most commonly used material is silicon, but germanium, gallium-arsenide and diamond are also useful in some applications. Integrated circuit technology allows the formation of high-density micron-scale electrodes on large (10–15 cm diameter) wafers, providing excellent position resolution. Furthermore, the density of silicon and its small ionization energy result in adequate signals with active layers only 100–300 μm thick, so the signals are also fast (typically tens of ns). Semiconductor detectors depend crucially on low-noise electronics (see Sec. 28.11), so the detection sensitivity is determined by signal charge and capacitance. For a comprehensive discussion of semiconductor detectors and electronics see Ref. 100.

Silicon detectors are p - n junction diodes operated at reverse bias. This forms a sensitive region depleted of mobile charge and sets up an electric field that sweeps charge liberated by radiation to the electrodes. Detectors typically use an asymmetric structure, e.g. a highly doped p electrode and a lightly doped n region, so that the depletion region extends predominantly into the lightly doped volume. The thickness of the depleted region is

$$W = \sqrt{2\epsilon(V + V_{bi})/Ne} = \sqrt{2\rho\mu\epsilon(V + V_{bi})} , \quad (28.19)$$

where V = external bias voltage

V_{bi} = “built-in” voltage (≈ 0.5 V for resistivities typically used in detectors)

N = doping concentration

e = electronic charge

ϵ = dielectric constant = $11.9 \epsilon_0 \approx 1$ pF/cm

ρ = resistivity (typically 1–10 k Ω cm)

μ = charge carrier mobility

= 1350 cm² V⁻¹ s⁻¹ for electrons

= 450 cm² V⁻¹ s⁻¹ for holes

or

$$W = 0.5 \left[\mu\text{m}/\sqrt{\Omega\text{-cm} \cdot \text{V}} \right] \times \sqrt{\rho(V + V_{bi})} \text{ for } n\text{-type material, and}$$

$$W = 0.3 \left[\mu\text{m}/\sqrt{\Omega\text{-cm} \cdot \text{V}} \right] \times \sqrt{\rho(V + V_{bi})} \text{ for } p\text{-type material.}$$

The conductive p and n regions together with the depleted volume form a capacitor with the capacitance per unit area

$$C = \epsilon/W \approx 1 \text{ [pF/cm]} / W . \quad (28.20)$$

In strip and pixel detectors the capacitance is dominated by the fringing capacitance. For example, the strip-to-strip fringing capacitance is ~ 1 – 1.5 pF cm⁻¹ of strip length at a strip pitch of 25–50 μm .

30 28. Particle detectors

Measurements on silicon photodiodes [101] show that for photon energies below 4 eV one electron-hole ($e-h$) pair is formed per incident photon. The mean energy E_i required to produce an $e-h$ pair peaks at 4.4 eV for a photon energy around 6 eV. It assumes a constant value, 3.67 eV at room temperature, above ~ 1.5 keV. It is larger than the bandgap energy because phonon excitation is required for momentum conservation. For minimum-ionizing particles, the most probable charge deposition in a 300 μm thick silicon detector is about 3.5 fC (22000 electrons). Since both electronic and lattice excitations are involved, the variance in the number of charge carriers $N = E/E_i$ produced by an absorbed energy E is reduced by the Fano factor F (about 0.1 in Si). Thus, $\sigma_N = \sqrt{FN}$ and the energy resolution $\sigma_E/E = \sqrt{FE_i/E}$. However, the measured signal fluctuations are usually dominated by electronic noise or energy loss fluctuations in the detector. Visible light can be detected with photon energies above the band gap. In optimized photodiodes quantum efficiencies $> 80\%$ for wavelengths between 400 nm and nearly 1 μm are achievable. UV-extended photodiodes have useful efficiency down to 200 nm.

Charge collection time decreases with increasing bias voltage, and can be reduced further by operating the detector with “overbias,” *i.e.* a bias voltage exceeding the value required to fully deplete the device. The collection time is limited by velocity saturation at high fields (approaching 10^7 cm/s at $E > 10^4$ V/cm); at an average field of 10^4 V/cm the collection time is about 15 ps/ μm for electrons and 30 ps/ μm for holes. In typical fully-depleted detectors 300 μm thick, electrons are collected within about 10 ns, and holes within about 25 ns.

Position resolution is limited by transverse diffusion during charge collection (typically 5 μm for 300 μm thickness) and by knock-on electrons. Resolutions of 2–4 μm (rms) have been obtained in beam tests. In magnetic fields, the Lorentz drift deflects the electron and hole trajectories and the detector must be tilted to reduce spatial spreading (see “Hall effect” in semiconductor textbooks).

Radiation damage occurs through two basic mechanisms:

1. Bulk damage due to displacement of atoms from their lattice sites. This leads to increased leakage current, carrier trapping, and build-up of space charge that changes the required operating voltage. Displacement damage depends on the nonionizing energy loss and the energy imparted to the recoil atoms, which can initiate a chain of subsequent displacements, *i.e.*, damage clusters. Hence, it is critical to consider both particle type and energy.
2. Surface damage due to charge build-up in surface layers, which leads to increased surface leakage currents. In strip detectors the inter-strip isolation is affected. The effects of charge build-up are strongly dependent on the device structure and on fabrication details. Since the damage is proportional to the absorbed energy (when ionization dominates), the dose can be specified in rad (or Gray) independent of particle type.

The increase in reverse bias current due to bulk damage is $\Delta I_r = \alpha\Phi$ per unit volume, where Φ is the particle fluence and α the damage coefficient ($\alpha \approx 3 \times 10^{-17}$ A/cm for minimum ionizing protons and pions after long-term annealing; $\alpha \approx 2 \times 10^{-17}$ A/cm for

1 MeV neutrons). The reverse bias current depends strongly on temperature

$$\frac{I_R(T_2)}{I_R(T_1)} = \left(\frac{T_2}{T_1}\right)^2 \exp\left[-\frac{E}{2k} \left(\frac{T_1 - T_2}{T_1 T_2}\right)\right] \quad (28.21)$$

where $E = 1.2$ eV, so rather modest cooling can reduce the current substantially (~ 6 -fold current reduction in cooling from room temperature to 0°C).

The space-charge concentration in high-resistivity n -type Si changes as

$$N \approx N_0 e^{-\delta\Phi} - \beta\Phi, \quad (28.22)$$

where N_0 is the initial donor concentration, $\delta \approx 6 \times 10^{-14} \text{ cm}^2$ determines donor removal, and $\beta \approx 0.03 \text{ cm}^{-1}$ describes acceptor creation. The acceptor states trap electrons, building up a negative space charge, which in turn requires an increase in the applied voltage to sweep signal charge through the detector thickness. This has the same effect as a change in resistivity, *i.e.*, the required voltage drops initially with fluence, until the positive and negative space charge balance and very little voltage is required to collect all signal charge. At larger fluences the negative space charge dominates, and the required operating voltage increases ($V \propto N$). The safe limit on operating voltage ultimately limits the detector lifetime. Strip detectors specifically designed for high voltages have been operated at bias voltages $>500\text{V}$. Since the effect of radiation damage depends on the electronic activity of defects, various techniques have been applied to neutralize the damage sites. For example, additional doping with oxygen increases the allowable charged hadron fluence roughly three-fold [102]. The increase in leakage current with fluence, on the other hand, appears to be unaffected by resistivity and whether the material is n or p -type.

Strip and pixel detectors have remained functional at fluences beyond 10^{15} cm^{-2} for minimum ionizing protons. At this damage level, charge loss due to recombination and trapping also becomes significant and the high signal-to-noise ratio obtainable with low-capacitance pixel structures extends detector lifetime. The occupancy of the defect charge states is strongly temperature dependent; competing processes can increase or decrease the required operating voltage. It is critical to choose the operating temperature judiciously (-10 to 0°C in typical collider detectors) and limit warm-up periods during maintenance. For a more detailed summary see Ref. 103 and the web-site of the ROSE collaboration at <http://RD48.web.cern.ch/rd48>.

Currently, the lifetime of detector systems is still limited by the detectors; in the electronics use of standard “deep submicron” CMOS fabrication processes with appropriately designed circuitry has increased the radiation resistance to fluences $> 10^{15} \text{ cm}^{-2}$ of minimum ionizing protons or pions. For a comprehensive discussion of radiation effects see Ref. 104.

28.11. Low-noise electronics

Revised August 2003 by H. Spieler (LBNL).

Many detectors rely critically on low-noise electronics, either to improve energy resolution or to allow a low detection threshold. A typical detector front-end is shown in Fig. 28.10.

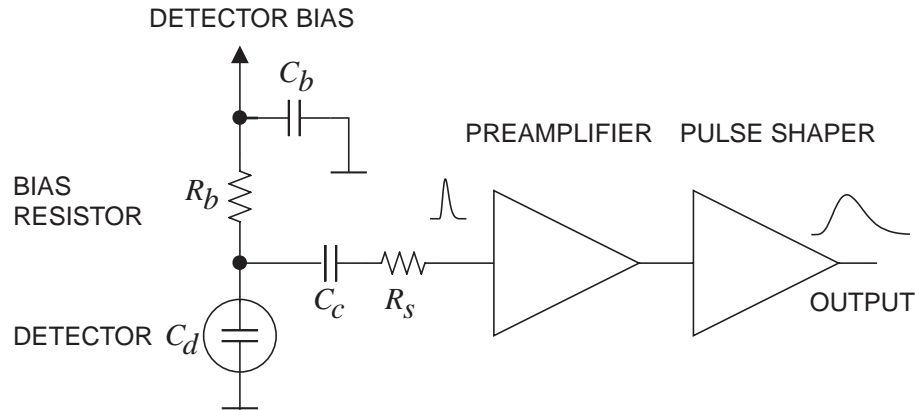


Figure 28.10: Typical detector front-end circuit.

The detector is represented by a capacitance C_d , a relevant model for most detectors. Bias voltage is applied through resistor R_b and the signal is coupled to the preamplifier through a blocking capacitor C_c . The series resistance R_s represents the sum of all resistances present in the input signal path, *e.g.* the electrode resistance, any input protection networks, and parasitic resistances in the input transistor. The preamplifier provides gain and feeds a pulse shaper, which tailors the overall frequency response to optimize signal-to-noise ratio while limiting the duration of the signal pulse to accommodate the signal pulse rate. Even if not explicitly stated, all amplifiers provide some form of pulse shaping due to their limited frequency response.

The equivalent circuit for the noise analysis (Fig. 28.11) includes both current and voltage noise sources. The leakage current of a semiconductor detector, for example, fluctuates due to electron emission statistics. This “shot noise” i_{nd} is represented by a current noise generator in parallel with the detector. Resistors exhibit noise due to thermal velocity fluctuations of the charge carriers. This noise source can be modeled either as a voltage or current generator. Generally, resistors shunting the input act as noise current sources and resistors in series with the input act as noise voltage sources (which is why some in the detector community refer to current and voltage noise as “parallel” and “series” noise). Since the bias resistor effectively shunts the input, as the capacitor C_b passes current fluctuations to ground, it acts as a current generator i_{nb} and its noise current has the same effect as the shot noise current from the detector. Any other shunt resistances can be incorporated in the same way. Conversely, the series resistor R_s acts as a voltage generator. The electronic noise of the amplifier is described fully by a combination of voltage and current sources at its input, shown as e_{na} and i_{na} .

Shot noise and thermal noise have a “white” frequency distribution, *i.e.* the spectral power densities $dP_n/df \propto di_n^2/df \propto de_n^2/df$ are constant with the magnitudes

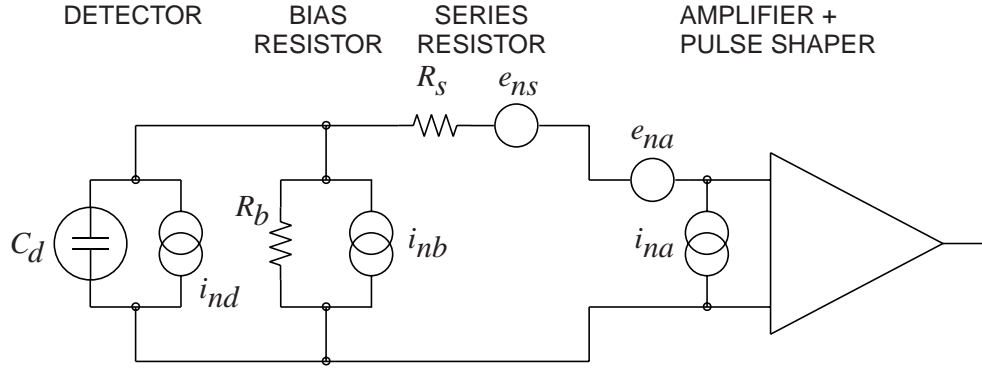


Figure 28.11: Equivalent circuit for noise analysis.

$$\begin{aligned}
 i_{nd}^2 &= 2eI_d , \\
 i_{nb}^2 &= \frac{4kT}{R_b} , \\
 e_{ns}^2 &= 4kTR_s ,
 \end{aligned} \tag{28.23}$$

where e is the electronic charge, I_d the detector bias current, k the Boltzmann constant and T the temperature. Typical amplifier noise parameters e_{na} and i_{na} are of order $\text{nV}/\sqrt{\text{Hz}}$ and $\text{pA}/\sqrt{\text{Hz}}$. Trapping and detrapping processes in resistors, dielectrics and semiconductors can introduce additional fluctuations whose noise power frequently exhibits a $1/f$ spectrum. The spectral density of the $1/f$ noise voltage is

$$e_{nf}^2 = \frac{A_f}{f} , \tag{28.24}$$

where the noise coefficient A_f is device specific and of order 10^{-10} – 10^{-12}V^2 .

A fraction of the noise current flows through the detector capacitance, resulting in a frequency-dependent noise voltage $i_n/(\omega C_d)$, which is added to the noise voltage in the input circuit. Since the individual noise contributions are random and uncorrelated, they add in quadrature. The total noise at the output of the pulse shaper is obtained by integrating over the full bandwidth of the system. Superimposed on repetitive detector signal pulses of constant magnitude, purely random noise produces a Gaussian signal distribution.

Since radiation detectors typically convert the deposited energy into charge, the system's noise level is conveniently expressed as an equivalent noise charge Q_n , which is equal to the detector signal that yields a signal-to-noise ratio of one. The equivalent noise charge is commonly expressed in Coulombs, the corresponding number of electrons, or the equivalent deposited energy (eV). For a capacitive sensor

$$Q_n^2 = i_n^2 F_i T_S + e_n^2 F_v \frac{C^2}{T_S} + F_v f A_f C^2 , \tag{28.25}$$

34 28. Particle detectors

where C is the sum of all capacitances shunting the input, F_i , F_v , and F_{vf} depend on the shape of the pulse determined by the shaper and T_s is a characteristic time, for example, the peaking time of a semi-gaussian pulse or the sampling interval in a correlated double sampler. The form factors F_i , F_v are easily calculated

$$F_i = \frac{1}{2T_s} \int_{-\infty}^{\infty} [W(t)]^2 dt, \quad F_v = \frac{T_s}{2} \int_{-\infty}^{\infty} \left[\frac{dW(t)}{dt} \right]^2 dt, \quad (28.26)$$

where for time-invariant pulse-shaping $W(t)$ is simply the system's impulse response (the output signal seen on an oscilloscope) with the peak output signal normalized to unity. For more details see Refs. [105–106].

A pulse shaper formed by a single differentiator and integrator with equal time constants has $F_i = F_v = 0.9$ and $F_{vf} = 4$, independent of the shaping time constant. The overall noise bandwidth, however, depends on the time constant, *i.e.* the characteristic time T_s . The contribution from noise currents increases with shaping time, *i.e.*, pulse duration, whereas the voltage noise decreases with increasing shaping time. Noise with a $1/f$ spectrum depends only on the ratio of upper to lower cutoff frequencies (integrator to differentiator time constants), so for a given shaper topology the $1/f$ contribution to Q_n is independent of T_s . Furthermore, the contribution of noise voltage sources to Q_n increases with detector capacitance. Pulse shapers can be designed to reduce the effect of current noise, *e.g.*, mitigate radiation damage. Increasing pulse symmetry tends to decrease F_i and increase F_v (*e.g.*, to 0.45 and 1.0 for a shaper with one CR differentiator and four cascaded integrators). For the circuit shown in Fig. 28.11,

$$Q_n^2 = \left(2eI_d + 4kT/R_b + i_{na}^2 \right) F_i T_s + (4kTR_s + e_{na}^2) F_v C_d^2 / T_s + F_{vf} A_f C_d^2. \quad (28.27)$$

As the characteristic time T_s is changed, the total noise goes through a minimum, where the current and voltage contributions are equal. Fig. 28.12 shows a typical example. At short shaping times the voltage noise dominates, whereas at long shaping times the current noise takes over. The noise minimum is flattened by the presence of $1/f$ noise. Increasing the detector capacitance will increase the voltage noise and shift the noise minimum to longer shaping times.

For quick estimates, one can use the following equation, which assumes an FET amplifier (negligible i_{na}) and a simple CR – RC shaper with time constants τ (equal to the peaking time):

$$(Q_n/e)^2 = 12 \left[\frac{1}{\text{nA} \cdot \text{ns}} \right] I_d \tau + 6 \times 10^5 \left[\frac{\text{k}\Omega}{\text{ns}} \right] \frac{\tau}{R_b} + 3.6 \times 10^4 \left[\frac{\text{ns}}{(\text{pF})^2 (\text{nV})^2 / \text{Hz}} \right] e_n^2 \frac{C^2}{\tau}. \quad (28.28)$$

Noise is improved by reducing the detector capacitance and leakage current, judiciously selecting all resistances in the input circuit, and choosing the optimum shaping time constant.

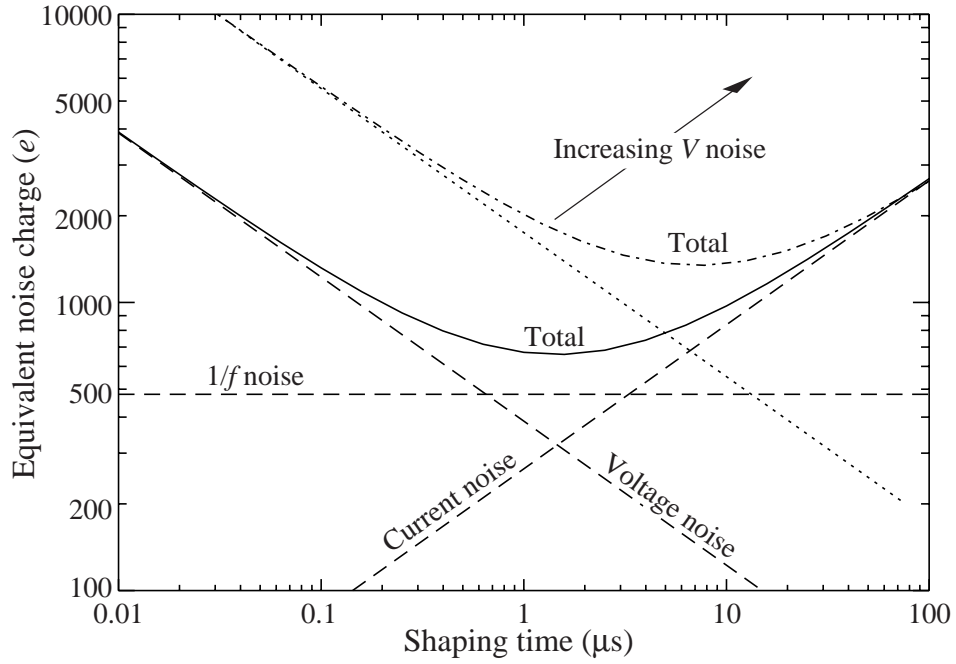


Figure 28.12: Equivalent noise charge *vs* shaping time. Changing the voltage or current noise contribution shifts the noise minimum. Increased voltage noise is shown as an example.

The noise parameters of the amplifier depend primarily on the input device. In field effect transistors, the noise current contribution is very small, so reducing the detector leakage current and increasing the bias resistance will allow long shaping times with correspondingly lower noise. In bipolar transistors, the base current sets a lower bound on the noise current, so these devices are best at short shaping times. In special cases where the noise of a transistor scales with geometry, *i.e.*, decreasing noise voltage with increasing input capacitance, the lowest noise is obtained when the input capacitance of the transistor is equal to the detector capacitance, albeit at the expense of power dissipation. Capacitive matching is useful with field-effect transistors, but not bipolar transistors. In bipolar transistors, the minimum obtainable noise is independent of shaping time, but only at the optimum collector current I_C , which does depend on shaping time.

$$Q_{n,\min}^2 = 4kT \frac{C}{\sqrt{\beta_{DC}}} \sqrt{F_i F_v} \quad \text{at} \quad I_c = \frac{kT}{e} C \sqrt{\beta_{DC}} \sqrt{\frac{F_v}{F_i} \frac{1}{T_S}}, \quad (28.29)$$

where β_{DC} is the DC current gain. For a CR - RC shaper and $\beta_{DC} = 100$,

$$Q_{n,\min}/e \approx 250 \sqrt{C/\text{pF}}. \quad (28.30)$$

Practical noise levels range from $\sim 1e$ for CCDs at long shaping times to $\sim 10^4 e$ in high-capacitance liquid argon calorimeters. Silicon strip detectors typically operate at $\sim 10^3 e$ electrons, whereas pixel detectors with fast readout provide noise of several hundred electrons.

36 28. Particle detectors

In timing measurements, the slope-to-noise ratio must be optimized, rather than the signal-to-noise ratio alone, so the rise time t_r of the pulse is important. The “jitter” σ_t of the timing distribution is

$$\sigma_t = \frac{\sigma_n}{(dS/dt)_{S_T}} \approx \frac{t_r}{S/N}, \quad (28.31)$$

where σ_n is the rms noise and the derivative of the signal dS/dt is evaluated at the trigger level S_T . To increase dS/dt without incurring excessive noise, the amplifier bandwidth should match the rise-time of the detector signal. The 10 to 90% rise time of an amplifier with bandwidth f_U is $0.35/f_U$. For example, an oscilloscope with 350 MHz bandwidth has a 1 ns rise time. When amplifiers are cascaded, which is invariably necessary, the individual rise times add in quadrature.

$$t_r \approx \sqrt{t_{r1}^2 + t_{r2}^2 + \dots + t_{rn}^2}$$

Increasing signal-to-noise ratio also improves time resolution, so minimizing the total capacitance at the input is also important. At high signal-to-noise ratios, the time jitter can be much smaller than the rise time. The timing distribution may shift with signal level (“walk”), but this can be corrected by various means, either in hardware or software [9].

For a more detailed introduction to detector signal processing and electronics see Ref. 100.

28.12. Calorimeters

28.12.1. Electromagnetic calorimeters:

Written August 2003 by R.-Y. Zhu (California Inst. of Technology).

The development of electromagnetic showers is discussed in the section on “Passage of Particles Through Matter” (Sec. 27 of this *Review*).

Formulae are given which approximately describe average showers, but since the physics of electromagnetic showers is well understood, detailed and reliable Monte Carlo simulation is possible. EGS4 [107] and GEANT [108] have emerged as the standards.

There are homogeneous and sampling electromagnetic calorimeters. In a homogeneous calorimeter the entire volume is sensitive, *i.e.*, contributes signal. Homogeneous electromagnetic calorimeters may be built with inorganic heavy (high- Z) scintillating crystals such as BGO, CsI, NaI, and PWO, non-scintillating Cherenkov radiators such as lead glass and lead fluoride, or ionizing noble liquids. Properties of commonly used inorganic crystal scintillators can be found in Table 28.2. A sampling calorimeter consists of an active medium which generates signal and a passive medium which functions as an absorber. The active medium may be a scintillator, an ionizing noble liquid, a gas chamber, or a semiconductor. The passive medium is usually a material of high density, such as lead, iron, copper, or depleted uranium.

The energy resolution σ_E/E of a calorimeter can be parametrized as $a/\sqrt{E} \oplus b \oplus c/E$, where \oplus represents addition in quadrature and E is in GeV. The stochastic term

a represents statistics-related fluctuations such as intrinsic shower fluctuations, photoelectron statistics, dead material at the front of the calorimeter, and sampling fluctuations. For a fixed number of radiation lengths, the stochastic term a for a sampling calorimeter is expected to be proportional to $\sqrt{t/f}$, where t is plate thickness and f is sampling fraction [109,110]. While a is at a few percent level for a homogeneous calorimeter, it is typically 10% for sampling calorimeters. The main contributions to the systematic, or constant, term b are detector non-uniformity and calibration uncertainty. In the case of the hadronic cascades discussed below, non-compensation also contributes to the constant term. One additional contribution to the constant term for calorimeters built for modern high-energy physics experiments, operated in a high-beam intensity environment, is radiation damage of the active medium. This can be minimized by developing radiation-hard active media [33] and by frequent *in situ* calibration and monitoring [32,110]. With effort, the constant term b can be reduced to below one percent. The term c is due to electronic noise summed over readout channels within a few Molière radii. The best energy resolution for electromagnetic shower measurement is obtained in total absorption homogeneous calorimeters, *e.g.* calorimeters built with heavy crystal scintillators. These are used when ultimate performance is pursued.

The position resolution depends on the effective Molière radius and the transverse granularity of the calorimeter. Like the energy resolution, it can be factored as $a/\sqrt{E} \oplus b$, where a is a few to 20 mm and b can be as small as a fraction of mm for a dense calorimeter with fine granularity. Electromagnetic calorimeters may also provide direction measurement for electrons and photons. This is important for photon-related physics when there are uncertainties in event origin, since photons do not leave information in the particle tracking system. Typical photon angular resolution is about $45 \text{ mrad}/\sqrt{E}$, which can be provided by implementing longitudinal segmentation [111] for a sampling calorimeter or by adding a preshower detector [112] for a homogeneous calorimeter without longitudinal segmentation.

Novel technologies have been developed for electromagnetic calorimetry. New heavy crystal scintillators, such as PWO, LSO:Ce, and GSO:Ce (see Sec. 28.2), have attracted much attention for homogeneous calorimetry. In some cases, such as PWO, it has received broad applications in high-energy and nuclear physics experiments. The “spaghetti” structure has been developed for sampling calorimetry with scintillating fibers as the sensitive medium. The “accordion” structure has been developed for sampling calorimetry with ionizing noble liquid as the sensitive medium. Table 28.5 provides a brief description of typical electromagnetic calorimeters built recently for high-energy physics experiments. Also listed in this table are calorimeter depths in radiation lengths (X_0) and the achieved energy resolution. Whenever possible, the performance of calorimeters *in situ* is quoted, which is usually in good agreement with prototype test beam results as well as EGS or GEANT simulations, provided that all systematic effects are properly included. Detailed references on detector design and performance can be found in Appendix C of reference [110] and Proceedings of the International Conference series on Calorimetry in Particle Physics.

Table 28.5: Resolution of typical electromagnetic calorimeters. E is in GeV.

Technology (Experiment)	Depth	Energy resolution	Date
NaI(Tl) (Crystal Ball)	$20X_0$	$2.7\%/E^{1/4}$	1983
Bi ₄ Ge ₃ O ₁₂ (BGO) (L3)	$22X_0$	$2\%/\sqrt{E} \oplus 0.7\%$	1993
CsI (KTeV)	$27X_0$	$2\%/\sqrt{E} \oplus 0.45\%$	1996
CsI(Tl) (BaBar)	$16\text{--}18X_0$	$2.3\%/E^{1/4} \oplus 1.4\%$	1999
CsI(Tl) (BELLE)	$16X_0$	1.7% for $E_\gamma > 3.5$ GeV	1998
PbWO ₄ (PWO) (CMS)	$25X_0$	$3\%/\sqrt{E} \oplus 0.5\% \oplus 0.2/E$	1997
Lead glass (OPAL)	$20.5X_0$	$5\%/\sqrt{E}$	1990
Liquid Kr (NA48)	$27X_0$	$3.2\%/\sqrt{E} \oplus 0.42\% \oplus 0.09/E$	1998
Scintillator/depleted U (ZEUS)	$20\text{--}30X_0$	$18\%/\sqrt{E}$	1988
Scintillator/Pb (CDF)	$18X_0$	$13.5\%/\sqrt{E}$	1988
Scintillator fiber/Pb spaghetti (KLOE)	$15X_0$	$5.7\%/\sqrt{E} \oplus 0.6\%$	1995
Liquid Ar/Pb (NA31)	$27X_0$	$7.5\%/\sqrt{E} \oplus 0.5\% \oplus 0.1/E$	1988
Liquid Ar/Pb (SLD)	$21X_0$	$8\%/\sqrt{E}$	1993
Liquid Ar/Pb (H1)	$20\text{--}30X_0$	$12\%/\sqrt{E} \oplus 1\%$	1998
Liquid Ar/depl. U (DØ)	$20.5X_0$	$16\%/\sqrt{E} \oplus 0.3\% \oplus 0.3/E$	1993
Liquid Ar/Pb accordion (ATLAS)	$25X_0$	$10\%/\sqrt{E} \oplus 0.4\% \oplus 0.3/E$	1996

28.12.2. Hadronic calorimeters: [110,113] The length scale appropriate for hadronic cascades is the nuclear interaction length, given very roughly by

$$\lambda_I \approx 35 \text{ g cm}^{-2} A^{1/3}. \quad (28.32)$$

Longitudinal energy deposition profiles are characterized by a sharp peak near the first interaction point (from the fairly local deposition of EM energy resulting from π^0 's produced in the first interaction), followed by a more gradual development with a maximum at

$$x/\lambda_I \equiv t_{\max} \approx 0.2 \ln(E/1 \text{ GeV}) + 0.7 \quad (28.33)$$

as measured from the front of the detector.

The depth required for containment of a fixed fraction of the energy also increases logarithmically with incident particle energy. The thickness of iron required for 95%

(99%) containment of cascades induced by single hadrons is shown in Fig. 28.13 [114]. Two of the sets of data are from large neutrino experiments, while the third is from a commonly-used parameterization. Depths as measured in nuclear interaction lengths presumably scale to other materials. From the same data it can be concluded that the requirement that 95% of the energy in 95% of the showers be contained requires 40 to 50 cm (2.4 to 3.0 λ_I) more material than for an average 95% containment. The transverse dimensions of hadronic showers also scale as λ_I , although most of the energy is contained in a narrow core.

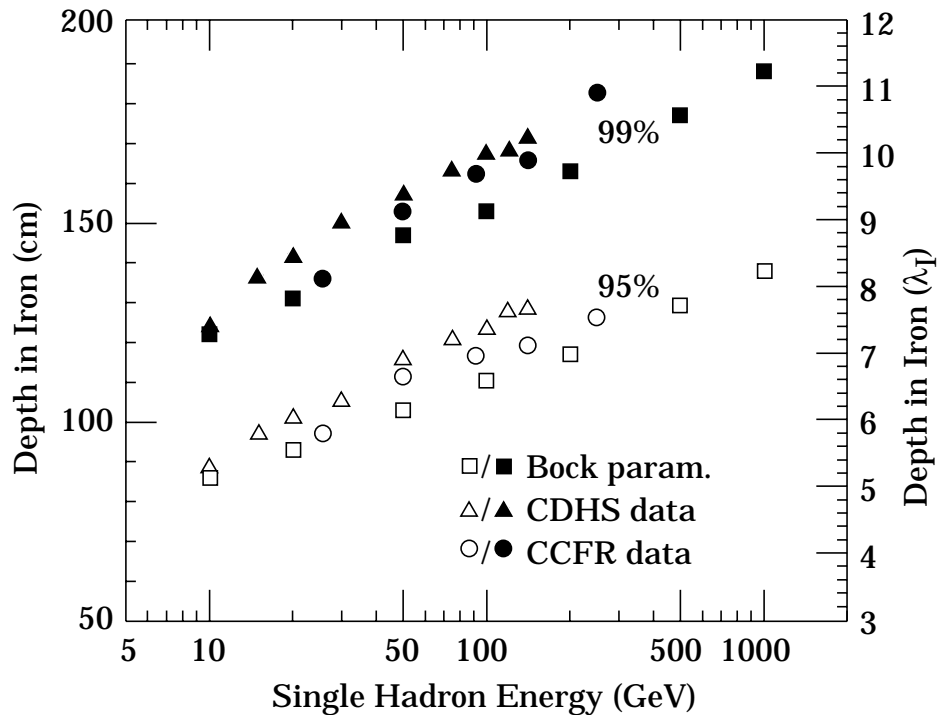


Figure 28.13: Required calorimeter thickness for 95% and 99% hadronic cascade containment in iron, on the basis of data from two large neutrino detectors and the parameterization of Bock *et al.* [114].

The energy deposit in a hadronic cascade consists of a prompt EM component due to π^0 production and a somewhat slower component mainly due to low-energy hadronic activity. An induction argument verified by Monte-Carlo simulations has shown that the fraction of hadronic energy in a cascade is $(E/E_0)^{m-1}$, where $0.80 \lesssim m \lesssim 0.85$ [115]. E_0 is about 1 GeV for incident pions, and the power-law description is approximately valid for incident energy E greater than a few tens of GeV. In general, the electromagnetic and hadronic energy depositions are converted to electrical signals with different efficiencies. The ratio of the conversion efficiencies is usually called the intrinsic e/h ratio. It follows in the power-law approximation the ratio of the responses for incident pions and incident electrons is given by “ π/e ” = $1 - (1 - h/e)(E/E_0)^{m-1}$. With or without the power-law approximation the response for pions is not a linear function of energy for $e/h \neq 1$. (But in any case, as the energy increases a larger and larger fraction of the energy is transferred

40 28. Particle detectors

to π^0 's, and “ $\pi/e \rightarrow 1$.”) If $e/h = 1.0$ the calorimeter is said to be *compensating*. If e/h differs from unity by more than 5% or 10%, detector performance is compromised because of fluctuations in the π^0 content of the cascades. This results in (a) a skewed signal distribution and (b) an almost-constant contribution to detector resolution which is proportional to the degree of noncompensation $|1 - h/e|$. The coefficient relating the size of the constant term to $|1 - h/e|$ is 14% according to FLUKA simulations [115], and 21% according to Wigmans' calculations [116]. (Wigmans now prefers a different approach to the “constant term” [110].)

The formula for “ π/e ” given above is valid for a large uniform calorimeter. Real calorimeters usually have an EM front structure which is different, and so modifications must be made in modeling the response.

In most cases e/h is greater than unity, particularly if little hydrogen is present or if the gate time is short. This is because much of the low-energy hadronic energy is “hidden” in nuclear binding energy release, low-energy spallation products, *etc.* Partial correction for these losses occurs in a sampling calorimeter with high- Z absorbers, because a disproportionate fraction of electromagnetic energy is deposited in the inactive region. For this reason, a fully sensitive detector such as scintillator or glass cannot be made compensating.

The average electromagnetic energy fraction in a high-energy cascade is smaller for incident protons than for pions; $E_0 \approx 2.6$ GeV rather than ≈ 1 GeV. As a result “ π/e ” > “ p/e ” (if $e/h > 1$) in a noncompensating calorimeter [115]. This difference has now been measured [117].

Circa 1990 compensation was thought to be very important in hadronic calorimeter design. Motivated very much by the work of Wigmans [116], several calorimeters were built with $e/h \approx 1 \pm 0.02$. These include

- ZEUS [118] 2.6 cm thick scintillator sheets sandwiched between 3.3 mm depleted uranium plates; a resolution of $0.35/\sqrt{E}$ was obtained;
- ZEUS prototype study [119], with 10 mm lead plates and 2.5 mm scintillator sheets; $0.44/\sqrt{E}$;
- D0 [120], where the sandwich cell consists of a 4–6 mm thick depleted uranium plate, 2.3 mm LAr, a G-10 signal board, and another 2.3 mm LAr gap; $45\%/\sqrt{E}$.

Approximately Gaussian signal distributions were observed.

More recently, compensation has not been considered as important, and, in addition, the new generation of calorimeters for LHC experiments operate in a different energy regime and can tolerate poorer resolution in return for simpler, deeper structures. For example, the ATLAS endcaps consist of iron plates with scintillating fiber readout [121]. The fraction of the structure consisting of low- Z active region (scintillator in this case) is much smaller than would be necessary to achieve compensation. Test beam results with these modules show a resolution of $\approx 46\%/\sqrt{E}$, and $e/h = 1.5$ – 1.6 .

28.12.3. Free electron drift velocities in liquid ionization sensors: Velocities as a function of electric field strength are given in Refs. 122–125 and are plotted in Fig. 28.14. Recent precise measurements of the free electron drift velocity in LAr have been published by W. Walkowiak [126]. These measurements were motivated by the design of the ATLAS electromagnetic calorimeter and inconsistencies in the previous literature. Velocities are systematically higher than those shown in Fig. 28.14.

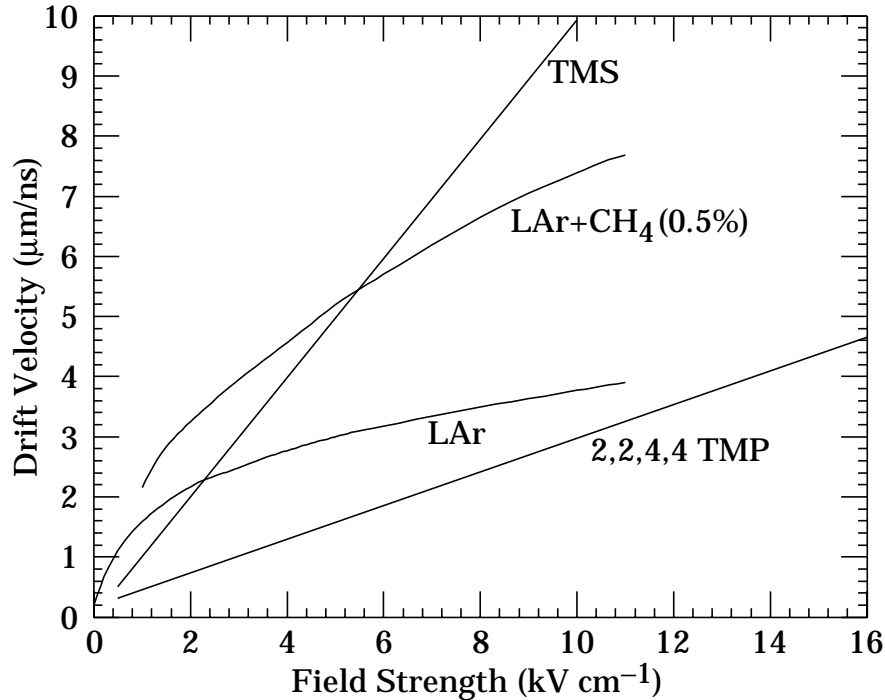


Figure 28.14: Electron drift velocity as a function of field strength for commonly used liquids.

28.13. Superconducting magnets for collider detectors

Revised October 2001 by R.D. Kephart (FNAL); revised September 2005 by A. Yamamoto (KEK)

28.13.1. Solenoid Magnets:

In all cases SI unit are assumed, so that the magnetic field, B , is in Tesla, the stored energy, E , is in joules, the dimensions are in meters, and $\mu_0 = 4\pi \times 10^{-7}$.

The magnetic field (B) in an ideal solenoid with a flux return iron yoke, in which the magnetic field is < 2 T, is given by

$$B = \mu_0 n I \quad (28.34)$$

where n is the number of turns/meter and I is the current. In an air-core solenoid, the central field is given by

$$B(0,0) = \mu_0 n I \frac{L}{\sqrt{L^2 + 4R^2}}, \quad (28.35)$$

42 28. Particle detectors

where L is the coil length and R is the coil radius.

In most cases, momentum analysis is made by measuring the circular trajectory of the passing particles according to $p = mv\gamma = qrB$, where p is the momentum, m the mass, q the charge, r the bending radius. The sagitta, s , of the trajectory is given by

$$s = qB\ell^2/8p, \quad (28.36)$$

where ℓ is the path length in the magnetic field. In a practical momentum measurement in colliding beam detectors, it is more effective to increase the magnetic volume than the field strength, since

$$dp/p \propto p/B\ell^2, \quad (28.37)$$

where ℓ corresponds to the solenoid coil radius R .

The energy stored in the magnetic field of any magnet is calculated by integrating B^2 over all space:

$$E = \frac{1}{2\mu_0} \int B^2 dV \quad (28.38)$$

If the coil thin, (which is the case if it is to superconducting coil), then

$$E \approx (B^2/2\mu_0)\pi R^2 L. \quad (28.39)$$

For a detector in which the calorimetry is outside the aperture of the solenoid, the coil must be thin in terms of radiation and absorption lengths. This usually means that the coil is superconducting and that the vacuum vessel encasing it is of minimum real thickness and fabricated of a material with long radiation length. There are two major contributors to the thickness of a thin solenoid:

- 1) The conductor consisting of the current-carrying superconducting material (usually NbTi/Cu) and the quench protecting stabilizer (usually aluminum) are wound on the inside of a structural support cylinder (usually aluminum also). The coil thickness scales as B^2R , so the thickness in radiation lengths (X_0) is

$$t_{\text{coil}}/X_0 = (R/\sigma_h X_0)(B^2/2\mu_0), \quad (28.40)$$

where t_{coil} is the physical thickness of the coil, X_0 the average radiation length of the coil/stabilizer material, and σ_h is the hoop stress in the coil [127]. $B^2/2\mu_0$ is the magnetic pressure. In large detector solenoids, the aluminum stabilizer and support cylinders dominate the thickness; the superconductor (NbTi/Cu) contributes a smaller fraction. The coil package including the cryostat typically contributes about 2/3 of the total thickness in radiation lengths.

- 2) Another contribution to the material comes from the outer cylindrical shell of the vacuum vessel. Since this shell is susceptible to buckling collapse, its thickness is determined by the diameter, length and the modulus of the material of which it is fabricated. The outer vacuum shell represents about 1/3 of the total thickness in radiation length.

28.13.2. Properties of collider detector magnets:

The physical dimensions, central field stored energy and thickness in radiation lengths normal to the beam line of the superconducting solenoids associated with the major collider are given in Table 28.6 [129]. Fig. 28.15 shows thickness in radiation lengths as a function of B^2R in various collider detector solenoids.

Table 28.6: Progress of superconducting magnets for particle physics detectors.

Experiment	Laboratory	B [T]	Radius [m]	Length [m]	Energy [MJ]	X/X_0	E/M [kJ/kg]
TOPAZ*	KEK	1.2	1.45	5.4	20	0.70	4.3
CDF	Tsukuba/Fermi	1.5	1.5	5.07	30	0.84	5.4
VENUS*	KEK	0.75	1.75	5.64	12	0.52	2.8
AMY*	KEK	3	1.29	3	40	‡	
CLEO-II	Cornell	1.5	1.55	3.8	25	2.5	3.7
ALEPH*	Saclay/CERN	1.5	2.75	7.0	130	2.0	5.5
DELPHI*	RAL/CERN	1.2	2.8	7.4	109	1.7	4.2
ZEUS	INFN/DESY	1.8	1.5	2.85	11	0.9	5.5
H1	RAL/DESY	1.2	2.8	5.75	120	1.8	4.8
BaBar	INFN/SLAC	1.5	1.5	3.46	27	‡	3.6
D0	Fermi	2.0	0.6	2.73	5.6	0.9	3.7
BELLE	KEK	1.5	1.8	4	42	‡	5.3
BES-III†	IHEP	1.0	1.475	3.5	9.5	‡	2.6
ATLAS-CS†	ATLAS/CERN	2.0	1.25	5.3	38	0.66	7.0
ATLAS-BT†	ATLAS/CERN	1	4.7–9.75	26	1080	(Toroid)	
ATLAS-ET†	ATLAS/CERN	1	0.825–5.35	5	2×250	(Toroid)	
CMS†	CMS/CERN	4	6	12.5	2600	‡	12

* No longer in service

† Detector under construction

‡ EM calorimeter is inside solenoid, so small X/X_0 is not a goal

The ratio of stored energy to cold mass (E/M) is a useful performance measure. It can also be expressed as the ratio of the stress, σ_h , to twice the equivalent density, ρ , in the coil [127]:

$$\frac{E}{M} = \frac{\int (B^2/2\mu_0) dV}{\rho V_{\text{coil}}} \approx \frac{\sigma_h}{2\rho} \quad (28.41)$$

The E/M ratio in the coil is approximately equivalent to H ,* the enthalpy of the coil, and it determines the average coil temperature rise after energy absorption in a quench:

$$E/M = H(T_2) - H(T_1) \approx H(T_2) \quad (28.42)$$

* The enthalpy, or heat content, is called H in the thermodynamics literature. It is not to be confused with the magnetic field intensity B/μ .

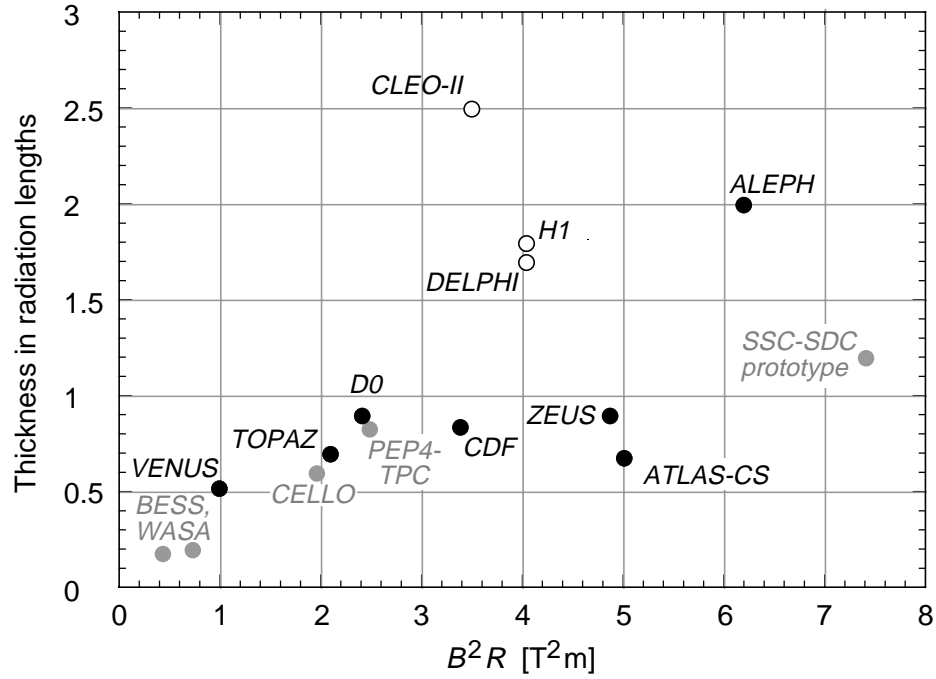


Figure 28.15: Magnet wall thickness in radiation length as a function of $B^2 R$ for various detector solenoids. Gray entries are for magnets not listed in Table 28.6. Open circles are for magnets not designed to be “thin.” The SSC-SDC prototype provided important R&D for LHC magnets.

where T_2 is the average coil temperature after the full energy absorption in a quench, and T_1 is the initial temperature. E/M ratios of 5, 10, and 20 kJ/kg correspond to ~ 65 , ~ 80 , and ~ 100 K, respectively. The E/M ratios of various detector magnets are shown in Fig. 28.16 as a function of total stored energy. One would like the cold mass to be as small as possible to minimize the thickness, but temperature rise during a quench must also be minimized. An E/M ratio as large as 12 kJ/kg is designed into the CMS solenoid, with the possibility that about half of the stored energy can go to an external dump resistor. Thus the coil temperature can be kept below 80 K if the energy extraction system work well. The limit is set by the maximum temperature that the coil design can tolerate during a quench. This maximum local temperature should be < 130 K (50 K + 80 K), so that thermal expansion effects in the coil are manageable.

28.13.3. Toroidal magnets:

Toroidal coils uniquely provide a closed magnetic field without the necessity of an iron flux-return yoke. Because no field exists at the collision point and along the beam line, there is, in principle, no effect on the beam. On the other hand, the field profile generally has $1/r$ dependence. The particle momentum may be determined by measurements of the deflection angle combined with the sagitta. The deflection (bending) power BL is

$$BL \approx \int_{R_i}^{R_0} \frac{B_i R_i dR}{R \sin \theta} = \frac{B_i R_i}{\sin \theta} \ln(R_0/R_i), \quad (28.43)$$

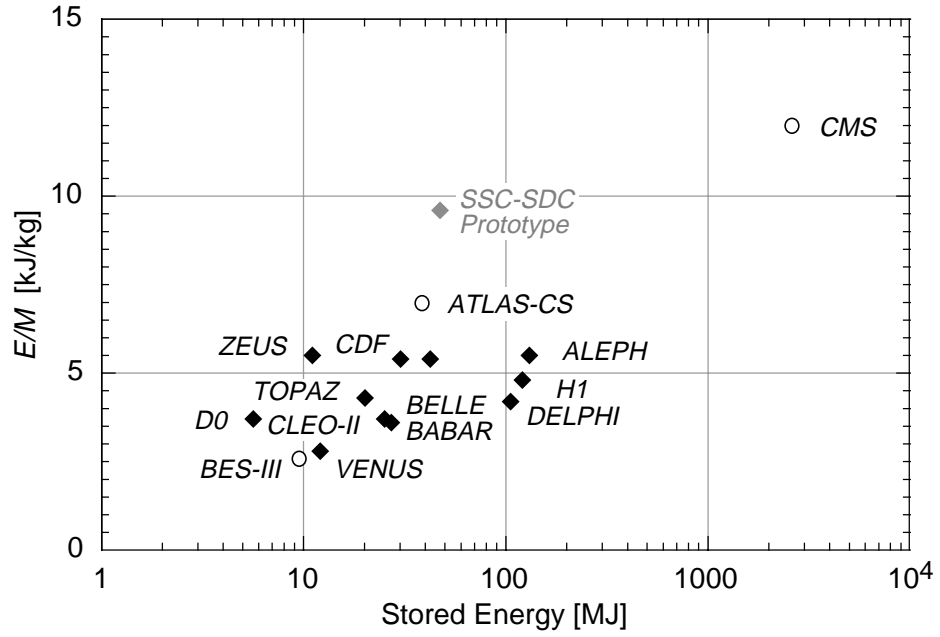


Figure 28.16: Ratio of stored energy to cold mass for thin detector solenoids. Open circles indicate magnets under construction.

where R_i is the inner coil radius, R_0 is the outer coil radius, and θ is the angle between the particle trajectory and the beam line axis. The momentum resolution given by the deflection may be expressed as

$$\frac{\Delta p}{p} \propto \frac{p}{BL} \approx \frac{p \sin \theta}{B_i R_i \ln(R_0/R_i)}. \quad (28.44)$$

The momentum resolution is better in the forward/backward (smaller θ) direction. The geometry has been found to be optimal when $R_0/R_i \approx 3-4$. In practical designs, the coil is divided into 6–12 lumped coils in order to have reasonable acceptance and accessibility. This causes the coil design to be much more complex. The mechanical structure needs to sustain the decentering force between adjacent coils, and the peak field in the coil is 3–5 times higher than the useful magnetic field for the momentum analysis [128].

28.14. Measurement of particle momenta in a uniform magnetic field [130,131]

The trajectory of a particle with momentum p (in GeV/c) and charge ze in a constant magnetic field \vec{B} is a helix, with radius of curvature R and pitch angle λ . The radius of curvature and momentum component perpendicular to \vec{B} are related by

$$p \cos \lambda = 0.3 z B R, \quad (28.45)$$

where B is in tesla and R is in meters.

The distribution of measurements of the curvature $k \equiv 1/R$ is approximately Gaussian. The curvature error for a large number of uniformly spaced measurements on the trajectory of a charged particle in a uniform magnetic field can be approximated by

$$(\delta k)^2 = (\delta k_{\text{res}})^2 + (\delta k_{\text{ms}})^2, \quad (28.46)$$

46 28. Particle detectors

where δk = curvature error

δk_{res} = curvature error due to finite measurement resolution

δk_{ms} = curvature error due to multiple scattering.

If many (≥ 10) uniformly spaced position measurements are made along a trajectory in a uniform medium,

$$\delta k_{\text{res}} = \frac{\epsilon}{L'^2} \sqrt{\frac{720}{N+4}}, \quad (28.47)$$

where N = number of points measured along track

L' = the projected length of the track onto the bending plane

ϵ = measurement error for each point, perpendicular to the trajectory.

If a vertex constraint is applied at the origin of the track, the coefficient under the radical becomes 320.

For arbitrary spacing of coordinates s_i measured along the projected trajectory and with variable measurement errors ϵ_i the curvature error δk_{res} is calculated from:

$$(\delta k_{\text{res}})^2 = \frac{4}{w} \frac{V_{ss}}{V_{ss}V_{s^2s^2} - (V_{ss^2})^2}, \quad (28.48)$$

where V are covariances defined as $V_{s^m s^n} = \langle s^m s^n \rangle - \langle s^m \rangle \langle s^n \rangle$ with $\langle s^m \rangle = w^{-1} \sum (s_i^m / \epsilon_i^2)$ and $w = \sum \epsilon_i^{-2}$.

The contribution due to multiple Coulomb scattering is approximately

$$\delta k_{\text{ms}} \approx \frac{(0.016)(\text{GeV}/c)z}{Lp\beta \cos^2 \lambda} \sqrt{\frac{L}{X_0}}, \quad (28.49)$$

where p = momentum (GeV/ c)

z = charge of incident particle in units of e

L = the total track length

X_0 = radiation length of the scattering medium (in units of length; the X_0 defined elsewhere must be multiplied by density)

β = the kinematic variable v/c .

More accurate approximations for multiple scattering may be found in the section on Passage of Particles Through Matter (Sec. 27 of this *Review*). The contribution to the curvature error is given approximately by $\delta k_{\text{ms}} \approx 8s_{\text{plane}}^{\text{rms}}/L^2$, where $s_{\text{plane}}^{\text{rms}}$ is defined there.

References:

1. *Experimental Techniques in High Energy Physics*, T. Ferbel (ed.) (Addison-Wesley, Menlo Park, CA, 1987).
2. Claus Grupen, *Particle Detectors*, Cambridge Monographs on Particle Physics, Nuclear Physics and Cosmology, # 5, Cambridge University Press (1996).

3. K. Kleinknecht, *Detectors for Particle Radiation*, Cambridge University Press (1998).
4. G.F. Knoll, *Radiation Detection and Measurement*, 3rd edition, John Wiley & Sons, New York (1999).
5. Dan Green, *The Physics of Particle Detectors*, Cambridge Monographs on Particle Physics, Nuclear Physics and Cosmology, # 12, Cambridge University Press (2000).
6. [Icarus Collaboration], ICARUS-TM/2001-09; LGNS-EXP 13/89 add 2-01.
7. E. Albert *et al.*, Nucl. Instrum. Methods **A409**, 70 (1998).
8. B. Aubert *et al.*, [BaBar Collaboration], Nucl. Instrum. Methods **A479**, 1 (2002).
9. H. Spieler, IEEE Trans. Nucl. Sci. **NS-29**, 1142 (1982).
10. J.B. Birks, *The Theory and Practice of Scintillation Counting*, (Pergamon, London, 1964).
11. D. Clark, Nucl. Instrum. Methods **117**, 295 (1974).
12. J.B. Birks, Proc. Phys. Soc. **A64**, 874 (1951).
13. B. Bengtson and M. Moszynski, Nucl. Instrum. Methods **117**, 227 (1974);
J. Bialkowski *et al.*, Nucl. Instrum. Methods **117**, 221 (1974).
14. *Proceedings of the Symposium on Detector Research and Development for the Superconducting Supercollider*, eds. T. Dombeck, V. Kelly, and G.P. Yost (World Scientific, Singapore, 1991).
15. I.B. Berlman, *Handbook of Fluorescence Spectra of Aromatic Molecules*, 2nd edition (Academic Press, New York, 1971).
16. C. Zorn, in *Instrumentation in High Energy Physics*, ed. F. Sauli, (1992, World Scientific, Singapore) pp. 218–279.
17. T. Foerster, Ann. Phys. **2**, 55 (1948).
18. J.M. Fluornoy, Conference on Radiation-Tolerant Plastic Scintillators and Detectors, K.F. Johnson and R.L. Clough editors, Rad. Phys. and Chem., **41** 389 (1993).
19. D. Horstman and U. Holm, *ibid*, 395.
20. D. Blomker *et al.*, Nucl. Instrum. Methods **A311**, 505 (1992);
J. Mainusch *et al.*, Nucl. Instrum. Methods **A312**, 451 (1992).
21. Conference on Radiation-Tolerant Plastic Scintillators and Detectors, K.F. Johnson and R.L. Clough editors, Rad. Phys. and Chem., **41** (1993).
22. S.R. Borenstein and R.C. Strand, IEEE Trans. Nuc. Sci. **NS-31(1)**, 396 (1984).
23. P. Sonderegger, Nucl. Instrum. Methods **A257**, 523 (1987).
24. S.A. Sedykh *et al.*, Nucl. Instrum. Methods **A455**, 346 (2000).
25. SCIFI 97: Conference on Scintillating Fiber Detectors, 1997 University of Notre Dame, Indiana, eds. A. Bross, R. Ruchti, and M. Wayne.
26. K.F. Johnson, Nucl. Instrum. Methods **A344**, 432 (1994).
27. C.M. Hawkes *et al.*, Nucl. Instrum. Methods **A292**, 329 (1990).
28. A. Lempicki *et al.*, Nucl. Instrum. Methods **A333**, 304 (1993);

48 28. Particle detectors

- G. Blasse, *Proceedings of the Crystal 2000 International Workshop on Heavy Scintillators for Scientific and Industrial Applications*, Chamonix, France, Sept. (1992), Edition Frontieres.
29. C. Melcher and J. Schweitzer, *Nucl. Instrum. Methods* **A314**, 212 (1992).
 30. K. Takagi and T. Fakazawa, *Appl. Phys. Lett.* **42**, 43 (1983).
 31. C. Kuntner *et al.*, *Nucl. Instrum. Methods* **A493**, 131 (2002).
 32. G. Gratta, H. Newman, and R.Y. Zhu, *Ann. Rev. Nucl. and Part. Sci.* **44**, 453 (1994).
 33. R.Y. Zhu, *Nucl. Instrum. Methods* **A413**, 297 (1998).
 34. M. Woods *et al.*, SPIN96 (QCD161:S921:1996) 843.
 35. A. Abashian *et al.*, *Nucl. Instrum. Methods* **A479**, 117 (2002).
 36. M. Shiozawa, [Super-Kamiokande Collaboration], *Nucl. Instrum. Methods* **A433**, 240 (1999).
 37. J. Litt and R. Meunier, *Ann. Rev. Nucl. Sci.* **23**, 1 (1973).
 38. D. Bartlett *et al.*, *Nucl. Instrum. Methods* **A260**, 55 (1987).
 39. B. Ratcliff, *Nucl. Instrum. Methods* **A502**, 211 (2003).
 40. M. Cavalli-Sforza *et al.*, "Construction and Testing of the SLC Cherenkov Ring Imaging Detector," *IEEE* **37**, N3:1132 (1990).
 41. E.G. Anassontzis *et al.*, "Recent Results from the DELPHI Barrel Ring Imaging Cherenkov Counter," *IEEE* **38**, N2:417 (1991).
 42. See the RICH Workshop series: *Nucl. Instrum. Methods* **A343**, 1 (1993); *Nucl. Instrum. Methods* **A371**, 1 (1996); *Nucl. Instrum. Methods* **A433**, 1 (1999); *Nucl. Instrum. Methods* **A502**, 1 (2003).
 43. H. Blood *et al.*, FERMILAB-PUB-76-051-EXP.
 44. L. Sulak, HUEP-252 Presented at the Workshop on Proton Stability, Madison, Wisc. (1978).
 45. K.S. Hirata *et al.*, *Phys. Lett.* **B205**, 416 (1988).
 46. S. Kasuga *et al.*, *Phys. Lett.* **B374**, 238 (1996).
 47. M.H. Ahn *et al.*, *Phys. Rev. Lett.* **90**, 041801 (2003).
 48. R.M. Bionta *et al.*, *Phys. Rev. Lett.* **51**, 27 (1983); [Erratum-*ibid.* **51**, 522 (1983)].
 49. R. Becker-Szendy *et al.*, *Nucl. Instrum. Methods* **A324**, 363 (1993).
 50. H. Ikeda *et al.*, UTLICEPP-82-04.
 51. K. Arisaka *et al.*, *J. Phys. Soc. Jap.* **54**, 3213 (1985).
 52. K.S. Hirata *et al.*, *Phys. Rev.* **D38**, 448 (1988).
 53. C. Athanassopoulos *et al.*, *Nucl. Instrum. Methods* **A388**, 149 (1997).
 54. Y. Fukuda *et al.*, *Nucl. Instrum. Methods* **A501**, 418 (2003).
 55. S.H. Ahn *et al.*, *Phys. Lett.* **B511**, 178 (2001).
 56. J. Boger *et al.*, *Nucl. Instrum. Methods* **A449**, 172 (2000).
 57. B. Dolgoshein *Nucl. Instrum. Methods* **A326**, 434 (1993).

58. X. Artru *et al.*, Phys. Rev. **D12**, 1289 (1975).
59. G.M. Garibian *et al.*, Nucl. Instrum. Methods **125**, 133 (1975).
60. G. Bassompierre *et al.*, Nucl. Instrum. Methods **411**, 63 (1998).
61. ALICE Collaboration, “Technical Design Report of the Transition Radiation Tracker,” CERN/LHCC/ 2001-021 (2001).
62. RD6 Collaboration, CERN/DRDC 90-38 (1990); CERN/DRDC 91-47 (1991); CERN/DRDC 93-46 (1993).
63. T. Kirn *et al.*, *Proceedings of TRDs for the 3rd millenium*, Workshop on advanced transition radiation detectors for accelerator and space applications, eds N. Giglietto and P. Spinelli, Frascati Physics Series, Vol. XXV, 161 (2002).
64. P. Spinelli *et al.*, Proceedings of “TRDs for the 3rd millenium”, Workshop on advanced transition radiation detectors for accelerator and space applications,” eds N. Giglietto and P. Spinelli, Frascati Physics Series, Vol. XXV, 177 (2002).
65. ATLAS Collaboration, ATLAS Inner Detector Technical Design Report, v 2, ATLAS TDR 5, CERN/LHCC/97-16 (30 April 1997).
66. ATLAS Collaboration, Detector and Physics Performance Technical Design Report, CERN/LHCC/99-14, 71 (1999).
67. B. Dolgoshein, Nucl. Instrum. Methods **252**, 137 (1986).
68. C.W. Fabjan *et al.*, Nucl. Instrum. Methods **185**, 119 (1981).
69. J. Cobb *et al.*, Nucl. Instrum. Methods **140**, 413 (1977).
70. A. Büngener *et al.*, Nucl. Instrum. Methods **214**, 261 (1983).
71. R.D. Appuhn *et al.*, Nucl. Instrum. Methods **263**, 309 (1988).
72. Y. Watase *et al.*, Nucl. Instrum. Methods **248**, 379 (1986).
73. R. Ansari *et al.*, Nucl. Instrum. Methods **263**, 51 (1988).
74. H.J. Butt *et al.*, Nucl. Instrum. Methods **252**, 483 (1986).
75. J.F. Detoeuf *et al.*, Nucl. Instrum. Methods **265**, 157 (1988).
76. M. Holder *et al.*, Nucl. Instrum. Methods **263**, 319 (1988).
77. H. Weidkamp, DiplomArbeit, Rhein-Westf. Tech. Hochschule Aachen (1984).
78. H. Grässler *et al.*, Proc. Vienna Wire Chamber Conference (1989).
79. T. Akesson *et al.*, Nucl. Instrum. Methods **A412**, 200 (1998).
80. F.F. Rieke and W. Prepejchal, Phys. Rev. **A6**, 1507 (1972).
81. L.G. Christophorou, “Atomic and molecular radiation physics” (Wiley, London 1991).
82. G. Charpak *et al.*, Nucl. Instrum. Methods **62**, 262 (1968).
83. R. Veenhof, GARFIELD program: simulation of gaseous detectors, version 6.32, CERN Program Library Pool W999 (W5050).
84. As representative examples see: B. Adeva *et al.*, Nucl. Instrum. Methods **A287**, 35 (1990).
85. As representative example see: A. Alexander *et al.*, Nucl. Instrum. Methods **A276**, 42 (1989).

50 28. Particle detectors

86. As representative examples see: F. Bedeschi *et al.*, Nucl. Instrum. Methods **A268**, 50 (1988);
Opal Collaboration: Nucl. Instrum. Methods **A305**, 275 (1991).
87. W. Blum and G. Rolandi, *Particle Detection with Drift Chambers*, Springer-Verlag (1994).
88. A. Peisert and F. Sauli, CERN-84-08 (Jul 1984).
89. R. Bellazzini and A. M. Spezziga, Rivista del Nuovo Cimento **17**, 1 (1994).
90. F. Sauli, Nucl. Instrum. Methods **A386**, 531 (1997).
91. Y. Giomataris, Ph. Rebougeard, J.P. Robert and G. Charpak, Nucl. Instrum. Methods **A376**, 29 (1996).
92. R. Santonico and R. Cardarelli, Nucl. Instrum. Methods **A187**, 377 (1981).
93. V. V. Parkhomchuck, Yu. N. Pestov, & N. V. Petrovykh, Nucl. Instrum. Methods **93**, 269 (1971).
94. P. Fonte, IEEE. Trans. Nucl. Sci. **49**, 881 (2002).
95. M. Abbrescia *et al.*, Nucl. Instrum. Methods **A394**, 13 (1997).
96. F. Anulli *et al.*, Nucl. Instrum. Methods **A552**, 276 (2005).
97. D.R. Nygren and J.N. Marx, "The Time Projection Chamber," Phys. Today **31**, 46 (1978).
98. F. Sauli, Nucl. Instrum. Methods **386**, 531 (1997).
99. Y. Giomataris, Ph. Rebougeard, J.P. Robert and G. Charpak, Nucl. Instrum. Methods **376**, 29 (1996).
100. H. Spieler, *Semiconductor Detector Systems*, Oxford Univ. Press, Oxford (2005) ISBN 0-19-852784-5.
101. F. Scholze *et al.*, Nucl. Instrum. Methods **A439**, 208 (2000).
102. G. Lindström *et al.*, Nucl. Instrum. Methods **A465**, 60 (2001).
103. G. Lindström *et al.*, Nucl. Instrum. Methods **A426**, 1 (1999).
104. A. Holmes-Siedle and L. Adams, *Handbook of Radiation Effects*, 2nd ed., Oxford 2002, ISBN 0-19-850733-X, QC474.H59 2001.
105. V. Radeka, IEEE Trans. Nucl. Sci. **NS-15/3**, 455 (1968);
V. Radeka, IEEE Trans. Nucl. Sci. **NS-21**, 51 (1974).
106. F.S. Goulding, Nucl. Instrum. Methods **100**, 493 (1972);
F.S. Goulding and D.A. Landis, IEEE Trans. Nucl. Sci. **NS-29**, 1125 (1982).
107. W.R. Nelson, H. Hirayama, and D.W.O. Rogers, "The EGS4 Code System," SLAC-265, Stanford Linear Accelerator Center (Dec. 1985).
108. R. Brun *et al.*, *GEANT3*, CERN DD/EE/84-1 (1987).
109. D. Hitlin *et al.*, Nucl. Instrum. Methods **137**, 225 (1976). See also W. J. Willis and V. Radeka, Nucl. Instrum. Methods **120**, 221 (1974), for a more detailed discussion.
110. R. Wigmans, *Calorimetry: Energy Measurement in Particle Physics*, Clarendon, Oxford (2000).

111. ATLAS Collaboration, *The ATLAS Liquid Argon Calorimeter Technical Design Report*, CERN/LHCC 96-41 (1996).
112. CMS Collaboration, *The CMS Electromagnetic Calorimeter Technical Design Report*, CERN/LHCC 97-33 (1997).
113. C. Leroy and P.-G. Rancoita, Rep. Prog. Phys. **63**, 505 (2000).
114. D. Bintinger, in *Proceedings of the Workshop on Calorimetry for the Supercollider*, Tuscaloosa, AL, March 13–17, 1989, edited by R. Donaldson and M.G.D. Gilchriese (World Scientific, Teaneck, NJ, 1989), p. 91;
R.K. Bock, T. Hansl-Kozanecka, and T.P. Shah, Nucl. Instrum. Methods **186**, 533 (1981).
115. T.A. Gabriel, D.E. Groom, P.K. Job, N.V. Mokhov, and G.R. Stevenson, Nucl. Instrum. Methods **A338**, 336 (1994).
116. R. Wigmans, Nucl. Instrum. Methods **A259**, 389 (1987);
R. Wigmans, Nucl. Instrum. Methods **A265**, 273 (1988).
117. N. Akchurian *et al.*, Nucl. Instrum. Methods **A408**, 380 (1998).
118. U. Behrens *et al.*, Nucl. Instrum. Methods **A289**, 115 (1990);
A. Bernstein *et al.*, Nucl. Instrum. Methods **A336**, 23 (1993).
119. E. Bernardi *et al.*, Nucl. Instrum. Methods **A262**, 229 (1987).
120. S. Abachi *et al.*, Nucl. Instrum. Methods **A324**, 53 (1993).
121. F. Ariztizabal *et al.*, Nucl. Instrum. Methods **A349**, 384 (1994).
122. E. Shibamura *et al.*, Nucl. Instrum. Methods **131**, 249 (1975).
123. T.G. Ryan and G.R. Freeman, J. Chem. Phys. **68**, 5144 (1978).
124. W.F. Schmidt, “Electron Migration in Liquids and Gases,” HMI B156 (1974).
125. A.O. Allen, “Drift Mobilities and Conduction Band Energies of Excess Electrons in Dielectric Liquids,” NSRDS-NBS-58 (1976).
126. W. Walkowiak, Nucl. Instrum. Methods **A449**, 288 (2000).
127. A. Yamamoto, Nucl. Instr. Meth. **A453**, 445 (2000).
128. T. Taylor, Phys. Scr. **23**, 459 (1980).
129. A. Yamamoto, Nucl. Instr. Meth. **A494**, 255 (2003).
130. R.L. Gluckstern, Nucl. Instrum. Methods **24**, 381 (1963).
131. V. Karimäki, Nucl. Instrum. Methods **A410**, 284 (1998).